

PAPER: Privacy-Preserving Convolutional Neural Networks using Low-Degree Polynomial Approximations and Structural Optimizations on Leveled FHE

Eduardo Chielle
New York University Abu Dhabi

Jinting Liu
New York University Shanghai

Michail Maniatakos
New York University Abu Dhabi

Manaar Alam
New York University Abu Dhabi

Jovan Kascelan
New York University Abu Dhabi

Abstract

Recent work using Fully Homomorphic Encryption (FHE) has made *non-interactive privacy-preserving inference* of deep Convolutional Neural Networks (CNN) possible. However, the performance of these methods remain limited by their heavy reliance on *bootstrapping*, a costly FHE operation applied across multiple layers, severely slowing inference. Moreover, they depend on *high-degree polynomial approximations* of non-linear activations, which increase multiplicative depth and reduce accuracy by 2–5% compared to plaintext ReLU models. In this work, we close the accuracy gap between FHE-based non-interactive CNNs and their plaintext counterparts, while also achieving faster inference than existing methods. We propose a *quadratic polynomial approximation* of ReLU, which achieves the theoretical minimum multiplicative depth for non-linear activations, together with a penalty-based training strategy. We further introduce *structural optimizations* that reduce the required FHE levels in CNNs by a factor of five compared to prior work, allowing us to *run deep CNN models under leveled FHE without bootstrapping*. To further accelerate inference and recover accuracy typically lost with polynomial approximations, we introduce parameter clustering along with a joint strategy of data layout and ensemble techniques. Experiments with VGG and ResNet models on CIFAR and Tiny-ImageNet datasets show that our approach achieves up to 4× faster private inference than prior work, with accuracy comparable to plaintext ReLU models.

1 Introduction

Machine Learning as a Service (MLaaS) is increasingly adopted across industries because it provides access to powerful models without requiring in-house development or maintenance [30]. However, it raises serious privacy concerns since models are often trained on proprietary or sensitive data [4, 28], and inference requires clients to share private information (e.g., medical or financial records) with external service providers. *Privacy-Preserving Machine Learning*

(PPML) addresses these risks using predominantly cryptographic methods, mainly secure *Multi-Party Computation* (MPC) [34] and *Fully Homomorphic Encryption* (FHE) [29], which protect both client data and provider models. Broadly, PPML methods fall into *interactive* and *non-interactive* categories [20]. Interactive PPML, based on MPC, requires the client and the service provider to jointly perform inference [11, 14, 16, 21, 24, 27]. It keeps computational costs relatively low but requires multiple communication rounds, which leads to high communication and bandwidth requirements. Non-interactive PPML, typically using FHE, adopts a fire-and-forget paradigm [5, 6, 13, 20, 23, 31], where the client encrypts inputs, the provider computes on ciphertexts, and the client decrypts the output. This reduces communication to a single round at the expense of heavy server-side computation. Despite the costs, non-interactive PPML is well-suited to third-party services because it eliminates client involvement during inference, supports clients with low-resource devices, and works in low-bandwidth settings. Motivated by these advantages, this work focuses on non-interactive PPML.

A key challenge in non-interactive PPML is implementing activation functions with cryptographic primitives. Activations are non-polynomial, and FHE natively supports only polynomial operations such as addition and multiplication. Existing work addresses this by approximating activations with single polynomials [11] or piecewise polynomials [21]. These approximations can be introduced before or after training. In *post-training approximation*, models are trained with standard activations (e.g., ReLU) and later replaced with high-precision polynomials. For example, MPCNN [20] uses minimax polynomials of orders {15, 15, 27}. In *pre-training approximation*, ReLU is replaced with a polynomial before training, which allows lower-degree approximations that reduce multiplicative depth and speed up inference. For example, shallow CNNs like CryptoNets [13] and LoLa [6], similar to LeNet-5 [19], achieve over 98% accuracy on MNIST with degree-2 polynomials. However, prior work [12] showed that training larger models (beyond AlexNet [18] or VGG-11 [33]) with such low-degree polynomials causes large approximation errors

that destabilize training. To date, PILLAR [11], which uses a degree-4 polynomial, is the lowest-degree approximation that generalizes to deep neural networks.

Implementing non-interactive PPML becomes increasingly difficult with deeper models. While *bootstrapping* enables evaluation of arbitrarily deep models, it is an expensive operation in FHE and remains the main scalability bottleneck. To avoid this cost, the literature has relied on *Leveled Fully Homomorphic Encryption* (LFHE). LFHE eliminates bootstrapping and allows faster private inference, but its computation is bounded by a fixed multiplicative depth determined by encryption parameters. As a result, the size and complexity of neural networks that can be evaluated under LFHE are strictly limited. The deepest CNNs shown to run with LFHE alone are AlexNet and VGG-11 [12]. Larger models have so far required bootstrapping. Consequently, modern deep CNNs have largely been regarded as incompatible with LFHE, and bootstrapping has become the default mechanism to address this limitation despite its high computational cost. For example, AutoFHE executes ResNet-32 inference with 8 or 19 bootstrapping layers in its lower- or higher-accuracy configuration, respectively [5], resulting in heavy computational costs.

This paper revisits the prevailing assumption that modern deep CNNs are incompatible with LFHE. We argue that heavy reliance on bootstrapping has obscured a large, underexplored optimization space. In FHE-based PPML, multiplicative depth directly determines the encryption parameters and the frequency of bootstrapping operations needed during evaluation, both of which have a dominant impact on inference time. Crucially, the multiplicative depth of CNNs is not an immutable property of the model architecture itself, but emerges from how its computation is realized. The network structure, degree of polynomial activations, linear transformations, data layout, function implementations, and placement of rescaling operations collectively govern depth. Careful analysis and optimization of these components and their interactions can substantially reduce multiplicative depth without changing model functionality. By aggressively minimizing multiplicative depth at every level of the model, rather than compensating for inefficiencies with bootstrapping, we show that deep CNNs can be evaluated efficiently under LFHE.

Guided by this philosophy, our goal is to design the *fastest non-interactive PPML framework that does not compromise accuracy*, under LFHE. We achieve this by combining four techniques: (i) low-degree polynomial activations that attain the theoretical minimum multiplicative depth for non-linear activation functions, (ii) a suite of structural optimizations that remove redundant operations, (iii) an ensemble-based strategy that recovers accuracy to near-ReLU levels, and (iv) a clustering technique to speed up the computation of convolutional layers. Importantly, while this work focuses on LFHE, the proposed techniques are not limited to it. They can be applied with FHE to run very deep models while substantially reducing the number of required bootstrapping operations.

Contributions: This work advances non-interactive PPML by enabling, for the first time, deep CNNs (e.g. ResNet-32) to run entirely under LFHE without bootstrapping, achieving accuracy comparable to plaintext ReLU models while outperforming prior work in both accuracy and inference time. Our contributions are fourfold:

- To the best of our knowledge, this is the first work to train deep CNNs effectively with *degree-2 polynomial activations*. We introduce a novel *penalty function* that ensures stable training and delivers accuracy on par with plaintext ReLU-based models. This achieves the theoretical minimum multiplicative depth of one for non-linear activations, whereas the lowest previously known stable alternative, PILLAR, requires a multiplicative depth of three (see §3).
- We propose three *structural optimization* techniques that reduce multiplicative depth of a model while preserving functional equivalence: (i) *Node Fusing*, which merges consecutive layers by folding normalization parameters into neighboring nodes, effectively eliminating the normalization layer; (ii) *Weight Redistribution*, which adjusts parameters so that coefficients of highest-order terms in polynomial activations and batch normalization, as well as divisors in pooling layers, normalize to one, removing redundant multiplications by constants; and (iii) *Tower Reuse*, which allows multiple multiplications within the same FHE level before rescaling. In the CKKS scheme used in this work [8], ciphertexts carry a scaling factor that grows with multiplications. Rescaling keeps ciphertext values within range but consumes a level. Since each level is represented by a modulus and homomorphic operations apply to all moduli, requiring fewer rescaling steps reduce the number of moduli, leading to faster homomorphic operations (see §4).
- We introduce a novel encoding strategy that utilizes unused ciphertext slots in FHE to pack multiple CNN model instances, enabling simultaneous *ensemble inference* within a single homomorphic evaluation. This approach enables the use of multiple independently trained models to recover accuracy lost to low-degree polynomial approximations through careful reuse of ciphertext–plaintext structures, albeit with additional inference overhead (see §5).
- To offset the additional private inference overhead from the choice of data layout that enables ensemble inference, we introduce a *parameter clustering* technique for convolutional layers that groups similar parameters to reduce redundant plaintext encodings and homomorphic computation. This technique recovers much of the lost inference speed while preserving model accuracy (see §5).

We evaluate our method on CIFAR [17] and Tiny-ImageNet [10] datasets, and show that it achieves up to $4\times$ faster private inference than prior work while achieving accuracy comparable to plaintext ReLU models (see §6).

2 Background

2.1 Leveled Fully Homomorphic Encryption

Homomorphic Encryption allows meaningful computations to be performed directly on encrypted data. In this work, we employ Residue Number System (RNS) variant [7] of the *Cheon-Kim-Kim-Song* (CKKS) [8] encryption scheme, which supports approximate arithmetic over encrypted complex numbers. CKKS is an FHE scheme based on the Ring-Learning With Errors (RLWE) problem [25]. The scheme operates across three spaces: message $\mathcal{M} = \mathbb{C}$, plaintext $\mathcal{P} = R_Q = \mathbb{Z}_Q[x]/(x^N + 1)$, and ciphertext $\mathcal{C} = R_Q \times R_Q$. *Encoding* maps a vector of $N/2$ numbers $\in \mathcal{M}$ into a degree- N polynomial $\in \mathcal{P}$, and *encryption* transforms a plaintext $\in \mathcal{P}$ into a ciphertext $\in \mathcal{C}$. In RNS-CKKS, the ciphertext modulus Q is decomposed into $\mathcal{L} + 1$ smaller primes $Q = \prod_{i=0}^{\mathcal{L}} q_i$, where \mathcal{L} denotes the level. A polynomial in R_Q is represented as $\mathcal{L} + 1$ polynomials in $R_{q_i} \forall i \in [0, \mathcal{L}] \cap \mathbb{Z}$, which allows computations using native 64-bit integer arithmetic.

CKKS supports homomorphic additions, multiplications, and rotations. Additions and multiplications act element-wise on the encoded vector, akin to SIMD operations. Rotations rotate the vector of $N/2$ encoded messages by a step $\in \mathbb{Z}_{N/2}$. During encoding, coefficients are scaled by a factor Δ , rounded to the nearest integers, and reduced modulo Q . Multiplying two encoded messages scales the result to Δ^2 , requiring *rescaling* to restore the scale to Δ . Rescaling removes one RNS modulus, reducing the level by 1. When the level reaches zero, *bootstrapping* can reset the ciphertext to a higher level, enabling unbounded computation. However, it is computationally expensive and avoided when possible. FHE without bootstrapping is called *Levelled Fully Homomorphic Encryption* (LFHE). In LFHE, the encryption parameters (N, Q) are chosen to provide the desired security and sufficient levels for a circuit with known multiplicative depth.

2.2 Challenges of Using Polynomial Activation

ReLU, defined as $ReLU(x) = \max(0, x)$, is one of the most widely used activation functions in deep learning due to its simplicity and computational efficiency. Its piecewise linear form provides the non-linearity required for neural networks to model complex patterns. However, in FHE settings, ReLU is difficult to implement because it relies on conditional branching, whereas FHE natively supports only additions and multiplications. As a result, any FHE-compatible ReLU must be a polynomial approximation. Higher-degree polynomials produce more accurate approximations but incur larger multiplicative depth. For a degree- d polynomial, the multiplicative depth is $\delta = \lceil \log_2 d \rceil + 1$, where the $(+1)$ accounts for coefficient multiplication. The lowest multiplicative depth for a ReLU approximation that generalizes to deep CNNs is achieved by PILLAR [11], which uses a degree-4 polynomial

$\sum_{i=0}^4 c_i x^i$ with $\delta = 3$. The theoretical minimum multiplicative depth for an activation function is one, attainable with a quadratic polynomial $x^2 + c_1 x + c_0$. Such polynomials have been successfully used in shallow CNNs like CryptoNets [13] and LoLa [6], but they fail in deeper models due to the escaping activation problem [12]. Moreover, polynomial approximations are accurate only over bounded input intervals. When used as direct substitutes for ReLU during training, they often cause a substantial drop in model accuracy [11, 12, 15]. This section focuses on two main reasons for this degradation: *escaping activations*, where intermediate layer outputs leave the polynomial’s approximation range, and *coefficient truncation*, arising from representing polynomial coefficients in fixed-point format to comply with FHE arithmetic.

Escaping Activations. Let $p_d(x) = \sum_{k=0}^d a_k x^k$ be a degree- d polynomial approximation of ReLU, with coefficients $a_k \in \mathbb{R}$, $\forall k \in \{0, \dots, d\}$. These coefficients are typically obtained by minimizing the least-squares error between $p_d(x)$ and ReLU on a finite set of real-valued points $\{x_i\}_{i=1}^N \subset [-c, c]$, for some parameter $c > 0$: $\min_{a_0, \dots, a_d} \sum_{i=1}^N (ReLU(x_i) - p_d(x_i))^2$. The resulting polynomial approximates ReLU well on $[-c, c]$ but can deviate substantially outside this range. ReLU exhibits piecewise linear growth:

$$ReLU(x) = \begin{cases} 0, & \text{if } x \leq 0 \\ x, & \text{if } x > 0 \end{cases} \Rightarrow ReLU(x) = O(x)$$

whereas any polynomial $p_d(x)$ with $d \geq 2$ grows as:

$$p_d(x) = a_d x^d + a_{d-1} x^{d-1} + \dots + a_1 x + a_0 = O(x^d)$$

This mismatch in growth rates leads to the *escaping activations* phenomenon [12]: as inputs propagate through the network, intermediate values can move outside $[-c, c]$, into regions where $p_d(x)$ no longer resembles ReLU. The resulting excessively large activations can cause exploding weights and rapid degradation of model performance, unless the training procedure is specifically adapted to control them.

Coefficient Truncation. In privacy-preserving FHE inference, all computations use fixed-point arithmetic with limited precision. This restriction limits both the range and resolution of representable values, constraining the domain of activation function inputs as well as the magnitudes of their polynomial approximation coefficients. The coefficients $\{a_k\}_{k=0}^d$ are usually obtained via floating-point least-squares fitting and then quantized for fixed-point evaluation under FHE: $\tilde{a}_k = \frac{\lfloor a_k 2^b \rfloor}{2^b}$, where $b \in \mathbb{N}$ is the number of fractional bits in the fixed-point format and $\lfloor \cdot \rfloor$ denotes rounding to the nearest integer. Least-squares fitting often produces small-magnitude coefficients, especially for higher-degree monomials. If $|a_k| < 2^{-(b+1)}$, the quantized coefficient \tilde{a}_k becomes zero, effectively removing the monomial x^k from the approximation. This *coefficient truncation* [11] changes the polynomial’s shape and can cause substantial deviation from the intended ReLU behavior, even within the approximation interval $[-c, c]$.

3 Training with Polynomial Approximation

3.1 Problem Setting

Dataset Configuration. Consider a dataset $\mathcal{D} = \{(x_i, y_i)\}_{i=1}^M$ for a multi-class classification task, where $x_i \in \mathbb{R}^n$ denotes the feature vector and $y_i \in \{1, \dots, K\}$ the corresponding label. The dataset contains M samples distributed across K classes.

ReLU Network. Let $f: \mathbb{R}^n \rightarrow \mathbb{R}^K$ denote an L -layer feed-forward neural network with ReLU activations. The network is parameterized by weight matrices $\{W^{(l)}\}_{l=1}^L$, where each $W^{(l)} \in \mathbb{R}^{n_l \times n_{l-1}}$ and n_l denotes the number of neurons in layer l . The network output is defined as $f(x) = h^{(L)}(x)$, where $h^{(0)}(x) = x$ and $h^{(l)}(x) = \text{ReLU}(W^{(l)}h^{(l-1)}(x))$ for all $1 \leq l \leq L$. The activation function $\text{ReLU}(z)$ is applied coordinate-wise as $\text{ReLU}(z) = \max(0, z)$.

Polynomial Network. We define a network $g: \mathbb{R}^n \rightarrow \mathbb{R}^K$ with the same architecture as f , but replacing each ReLU activation with a degree- d polynomial $p_d(z) = \sum_{k=0}^d a_k z^k$ that approximates the ReLU function on a bounded interval $[-c, c]$. The polynomial coefficients $\{a_k\}_{k=0}^d$ are chosen so that the maximum approximation error satisfies: $\max_{z \in [-c, c]} |\text{ReLU}(z) - p_d(z)| \leq \epsilon$, where $\epsilon > 0$ is a prescribed approximation tolerance. The resulting network output is given by $g(x) = h_{p_d}^{(L)}(x)$, where $h_{p_d}^{(0)}(x) = x$ and $h_{p_d}^{(l)}(x) = p_d(W^{(l)}h_{p_d}^{(l-1)}(x))$ for all $1 \leq l \leq L$.

Challenges. While polynomial activations enable compatibility with FHE schemes, they introduce several non-trivial optimization challenges, most notably *escaping activations* and *coefficient truncation*, as discussed in §2.2. Addressing these issues typically requires careful selection of the polynomial degree d , the approximation interval $[-c, c]$, and coefficient bounds b , together with regularization strategies designed to ensure that intermediate activations remain within the valid approximation range throughout training.

3.2 Training Strategy

Quantization-Aware Polynomial Fitting. To avoid precision loss due to coefficient truncation, we incorporate fixed-point constraints directly into coefficient estimation procedure using *quantization-aware polynomial fitting* [11]. Given an approximation interval $[-c, c]$ and fixed-point precision with b fractional bits, we define a quantized input domain for polynomial fitting as: $X = \{x \in [-c, c] \mid x = k \cdot 2^{-b}, k \in \mathbb{Z}\}$. For each input $x_i \in X$, we compute scaled ReLU outputs $Y_i = 2^b \cdot \text{ReLU}(x_i)$ so that regression targets are integers, which reduces risk of precision loss during optimization. We construct a matrix $B \in \mathbb{R}^{M \times (d+1)}$ with entries $B_{i,k} = x_i^k$ for $0 \leq k \leq d$. The coefficients $A = [a_0, \dots, a_d]^\top \in \mathbb{Z}^{d+1}$ are obtained by solving bounded integer least-squares problem: $\min_{A \in \mathbb{Z}^{d+1}} \|BA - Y\|_2^2$ subject to $a_k \in [-2^{b-1}, 2^{b-1} - 1]$. The resulting fixed-point polynomial is $p_d(x) = \sum_{k=0}^d (a_k/2^b)x^k$.

Activation Regularization. To avoid escaping activations, we introduce a *regularization strategy* that constrains the inputs to polynomial activation functions (i.e., the pre-activations) to remain within the valid approximation interval $[-c, c]$. The classification loss supervises only the final output and provides no mechanism to limit intermediate pre-activation values. Hence, minimizing it alone does not prevent pre-activations from drifting outside the interval $[-c, c]$, where the polynomial diverges from ReLU and destabilizes training. We introduce a layer-wise penalty that penalizes out-of-range pre-activations. For a mini-batch $\mathcal{B} \subset \mathcal{D}$, the following training loss is minimized:

$$\mathcal{L}_{\mathcal{B}} = \underbrace{\frac{1}{|\mathcal{B}|} \sum_{(x,y) \in \mathcal{B}} \ell_{\text{CE}}(g(x), y)}_{\text{classification loss}} + \underbrace{\zeta \frac{1}{L} \sum_{l=1}^L \left\| z_p^{(l)} - \text{clip}\left(z_p^{(l)}; [-c, c]\right) \right\|_2}_{\text{clip-range penalty}} \quad (1)$$

where ℓ_{CE} is the *cross-entropy loss*, $z_p^{(l)}$ are pre-activations at layer l , i.e., outputs of affine transformations $W^{(l)}h_{p_d}^{(l-1)}(x)$ before the polynomial activation. The function $\text{clip}(z; [-c, c])$ is applied element-wise and defined as: $\text{clip}(z; [-c, c])_i = \max(-c, \min(z_i, c))$. The second loss term penalizes pre-activations that lie outside $[-c, c]$, with strength controlled by the regularization parameter $\zeta > 0$. See §A for a proof of the penalty function’s correctness. Training can still become unstable for two reasons: (i) in early epochs pre-activations can grow unbounded before the model learns to contain them and (ii) using full regularization weight ζ from the start can let the penalty dominate and destabilize optimization. As additional strategies, we also consider *clipping pre-activations during training* and introducing a *warm-up schedule* for ζ .

Pre-Activation Clipping. During early training stages, network weights remain close to their random initialization, and the optimization process does not immediately constrain the pre-activation values to lie within the target approximation interval $[-c, c]$. As a result, unbounded pre-activations may arise before the model learns to keep them within range, causing training instability that can degrade model behavior. To prevent this, we restrict pre-activations to the interval $[-c, c]$ before evaluating the polynomial activation, which is achieved through a *clipping strategy* $\text{clip}(z; [-c, c])$ [11]:

$$h_{p_d}^{(l)}(x) = p_d\left(\text{clip}\left(W^{(l)}h_{p_d}^{(l-1)}(x); [-c, c]\right)\right).$$

Importantly, this *clipping operation is applied only during training* to stabilize learning. It is performed after computing the clip-range penalty to ensure that gradients from the regularization term, which encourages the network to keep pre-activations within the approximation interval $[-c, c]$, are preserved and not masked by the clipping. At inference time, the

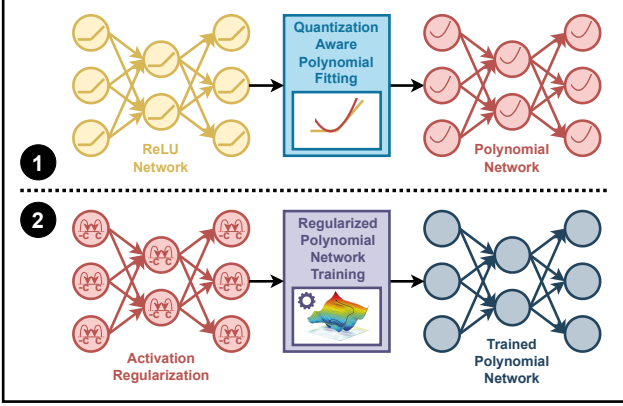


Figure 1: Overview of the two-stage training pipeline of a neural network with polynomial approximation. **1** A ReLU network is approximated using *quantization-aware polynomial fitting* to obtain an initial polynomial network. **2** The polynomial network is then trained through *regularized polynomial network training*, consisting of *activation regularization*, *pre-activation clipping*, and *warm-up scheduling*, to ensure stable convergence.

clipping function is removed: $h_{p_d}^{(l)}(x) = p_d \left(W^{(l)} h_{p_d}^{(l-1)}(x) \right)$. The model, having learned to constrain pre-activations during training, is expected to remain within the approximation interval without explicit clipping at inference.

Regularization Warm-up. While activation regularization and pre-activation clipping are both necessary for training stability, applying the full regularization strength from the outset can lead to numerical instability, particularly in larger models. In the early epochs, many pre-activation values lie outside the target interval $[-c, c]$ across several layers. The clip-range penalty adds a contribution from every such layer, so the penalty term becomes very large. In extreme cases, this can cause the total loss to become numerically undefined.

To address this issue, the regularization strength ζ is progressively increased over the initial epochs, which is implemented through a *regularization warm up schedule* [11]. Let T_{warm} denote the total number of warm-up epochs. For each epoch t , we define a *time-dependent regularization weight* ζ_t :

$$\zeta_t = \begin{cases} \alpha_t \cdot \zeta & \text{if } t \leq T_{warm} \\ \zeta & \text{if } t > T_{warm} \end{cases},$$

where $\{\alpha_t\}_{t=1}^{T_{warm}}$ is a fixed sequence of scaling factors satisfying $0 < \alpha_1 < \dots < \alpha_{T_{warm}} < 1$. In practice, we empirically find that setting $T_{warm} = 4$ provides a stable convergence. We use a predefined sequence of scaling factors: $\alpha = \left\{ \frac{1}{100}, \frac{1}{50}, \frac{1}{10}, \frac{1}{5} \right\}$, which produces the epoch-wise regularization strength: $\zeta_t \in \left\{ \frac{\zeta}{100}, \frac{\zeta}{50}, \frac{\zeta}{10}, \frac{\zeta}{5}, \zeta, \zeta, \dots \right\}$. This warm-up schedule ensures that the regularization penalty is introduced progressively in the initial training epochs without suffering from exploding loss values. Figure 1 shows an overview of the training process with polynomial approximation.

4 Structural Optimizations

4.1 Node Fusing

Our first optimization is *node fusing*, which merges consecutive computational nodes into a single equivalent function. This reduces both the number of operations and multiplicative depth. Formally, two sequential nodes $F(G(x))$ are replaced with $H(x)$ such that $F(G(x)) = H(x)$, with $H(x)$ more efficient to evaluate. Following this principle, we present four cases where compositions are fused into a single, more efficient operation, as illustrated in Figure 2. Since all cases involve batch normalization, recall its polynomial form:

$$B(x) = b_1x + b_0$$

with $b_1 = \frac{\gamma}{\sigma}$, $b_0 = \beta_b - b_1\mu$, where μ , σ are the input mean and standard deviation, and γ , β_b are learnable parameters. We outline the fusion cases below. See §B.1 for full derivations.

Case 1: $P(B(x)) \mapsto P(x)$. When a polynomial activation $P(\cdot)$ follows batch normalization, the two can be fused into a single quadratic polynomial. If $P(x) = c_2x^2 + c_1x + c_0$, then $P(B(x)) = p_2x^2 + p_1x + p_0$, with fused coefficients $p_2 = b_1^2c_2$, $p_1 = b_1(2b_0c_2 + c_1)$, $p_0 = b_0^2c_2 + b_0c_1 + c_0$.

Case 2: $B(C(x)) \mapsto C(x)$. Batch normalization can be fused into a preceding convolution [26]. A convolution is given by $C(x) = \sum_i w_i x_i + \beta_c$, where w_i are the weights and β_c is the bias. The fused form becomes a single convolution $B(C(x)) = \sum_i \omega_i x_i + \alpha$, with fused coefficients $\omega_i = b_1 w_i$, $\alpha = b_1 \beta_c + b_0$.

Case 3: $P(B_X(x) + B_Y(y)) \mapsto S(x, y)$. In residual networks, skip connections often merge two batch-normalized branches by summing them before applying an activation $P(\cdot)$. Specifically, $P(B_X(x) + B_Y(y))$. Here, B_X and B_Y are independent batch normalization layers to inputs x and y , respectively. This structure can be fused into a single quadratic bivariate polynomial $S(x, y) = d_{X2}x^2 + d_{Y2}y^2 + d_{XY}xy + d_{X1}x + d_{Y1}y + d_0$, with coefficients $d_{X2} = c_2b_{X1}^2$, $d_{Y2} = c_2b_{Y1}^2$, $d_{XY} = 2c_2b_{X1}b_{Y1}$, $d_{X1} = b_{X1}(2c_2(b_{X0} + b_{Y0}) + c_1)$, $d_{Y1} = b_{Y1}(2c_2(b_{X0} + b_{Y0}) + c_1)$, $d_0 = c_2(b_{X0} + b_{Y0})^2 + c_1(b_{X0} + b_{Y0}) + c_0$.

Case 4: $P(B_X(x) + y) \mapsto S(x, y)$. Some skip connections use identity shortcuts, where the input y is added directly to the batch-normalized branch $B_X(x)$ before applying the activation. This structure can be fused into a quadratic bivariate polynomial $S(x, y) = d_{X2}x^2 + d_{Y2}y^2 + d_{XY}xy + d_{X1}x + d_{Y1}y + d_0$, with $d_{X2} = c_2b_{X1}^2$, $d_{Y2} = c_2$, $d_{XY} = 2c_2b_{X1}$, $d_{X1} = b_{X1}(2c_2b_{X0} + c_1)$, $d_{Y1} = 2c_2b_{X0} + c_1$, $d_0 = c_2b_{X0}^2 + c_1b_{X0} + c_0$.

Node fusing collapses batch normalizations, activation functions, convolutional layers, and skip connections into single fused polynomials, eliminating redundant nodes and reducing multiplicative depth. This technique is applied after model training but before inference, transforming the model structure into a functionally equivalent, more efficient form.

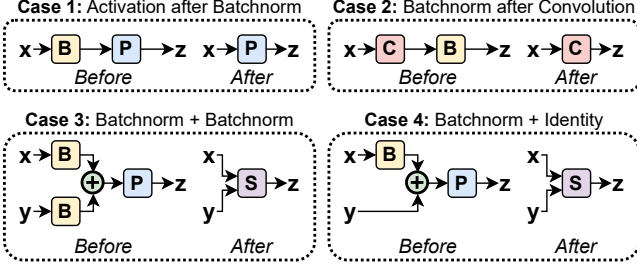


Figure 2: Illustration of node fusing cases. Nodes are batch normalization (B), convolution (C), univariate (P) and bivariate (S) polynomial activations, and addition (\oplus).

4.2 Weight Redistribution

Our second optimization is *weight redistribution*, a technique that redistributes weights across the network while maintaining functional equivalence. The goal is to reduce the multiplicative depth of selected operations by one. It specifically targets average pooling, batch normalization, and polynomial activation. For average pooling, redistribution eliminates the normalization step by setting the divisor to one. For polynomial functions, coefficients are normalized so that the highest-order coefficient is set to one. For example, the polynomial activation $c_2x^2 + c_1x + c_0$ is transformed into $x^2 + \bar{c}_1x + \bar{c}_0$, reducing its multiplicative depth from two to one, *the theoretical minimum for an activation function*. These transformations alone break model equivalence. To maintain it, other nodes in the network must compensate for the redistributed weights. We refer to the nodes that initiate redistribution as *donors*, and to nodes that adjust their parameters to restore equivalence as *receivers*. We represent the network as a directed graph and traverse it to identify all eligible donor nodes. For each donor, redistribution can be applied either *forward* or *backward*, affecting receivers among the donor’s successors or predecessors, respectively, as illustrated in Figure 3.

Update Forward.

Donors. We first consider donor updates in the forward direction. Our goal is to construct a normalized function $\bar{F}(x)$ such that $\nu\bar{F}(x) = F(x)$, where $F(x)$ is the original donor function and ν is the update term to be propagated to receivers.

Average Pooling. The average pooling operation is given by $\mu(x) = k^{-1} \sum_i x_i$, where k is the kernel size. In the normalized function we set $k = 1$, reducing the operation to $\bar{\mu}(x) = \sum_i x_i$. Thus, for the equality to be true, we have $\nu = k^{-1}$.

Polynomial Functions. Batch normalization and polynomial activation are polynomial functions. For a univariate polynomial $P(x) = \sum_{i=0}^d c_i x^i$ of degree d , and a normalized polynomial $\bar{P}(x) = x^d + \sum_{i=0}^{d-1} \bar{c}_i x^i$, where \bar{c}_i are the normalized coefficients, we have $\nu = c_d$ and $\bar{c}_i = c_i \nu^{-1}$ for $\nu\bar{P}(x) = P(x)$ to hold. The extension to the bivariate polynomial activation is analogous and deferred to §B.2.

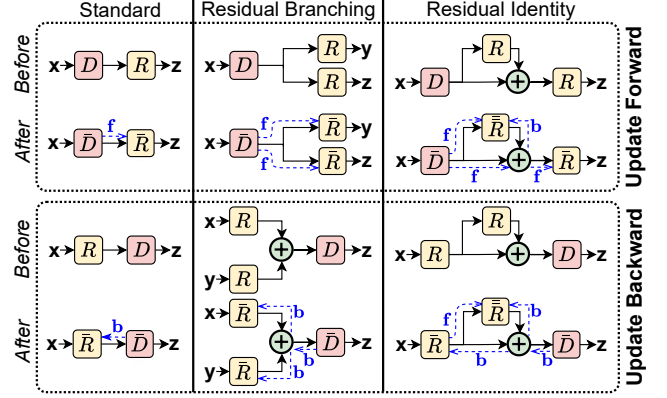


Figure 3: Illustration of weight redistribution cases. D represents a donor and R a receiver. The number of bars ($\bar{\cdot}$) on a D or R represents the number of updates the node received. \mathbf{f} represents a forward and \mathbf{b} a backward update.

Receivers. After a donor update, receivers must be adjusted to maintain model equivalence. The original composed function is $G(F(\cdot))$, where $F(\cdot)$ is the donor and $G(\cdot)$ is the receiver. Updating the donor to $\bar{F}(\cdot)$ without compensating the receiver results in $G(\nu^{-1}F(\cdot))$, breaking model equivalence. To restore it, we modify the receiver to $\bar{G}(\cdot)$ so that $\bar{G}(\bar{F}(\cdot)) = \bar{G}(\nu^{-1}F(\cdot)) = G(F(\cdot))$. Receivers fall into two categories: kernel functions and polynomial functions.

Kernel Functions. Convolution, linear, and average pooling share the form $K(x) = \sum_i w_i x_i + \beta$ ($w_i = k^{-1}$ and $\beta = 0$ for average pooling). To maintain model equivalence, we must update the kernel function such that $\bar{K}(\nu^{-1}x) = K(x)$ is valid. For that, we set $\bar{w}_i = w_i \nu$ and keep $\bar{\beta} = \beta$.

Polynomial Functions. Batch normalization and polynomial activation update as $\bar{P}(\nu^{-1}x) = P(x)$, implying that $\bar{c}_i = c_i \nu^i$. For the bivariate polynomial activation, in $\bar{S}(\nu^{-1}x, y) = S(x, y)$ the index i corresponds to the exponent of x , while in $\bar{S}(x, \nu^{-1}y) = S(x, y)$ it corresponds to the exponent of y .

Update Backward.

Donors. Backward updates are essentially the inverse of forward updates. For average pooling, the update is identical, since $\bar{\mu}(\nu x) = \nu \bar{\mu}(x)$, while for polynomial donors, it must hold that $\bar{P}(\nu x) = P(x)$; hence, $\nu = c_d^{1/d}$ and $\bar{c}_i = c_i \nu^{-i}$.

Receivers. To preserve model equivalence, receivers must satisfy $\bar{G}(x) = \nu G(x)$. Kernel receivers update as $\bar{K}(x) = \nu K(x)$, which implies that $\bar{w}_i = w_i \nu$ and $\bar{\beta} = \beta \nu$. And polynomial receivers update according to $\bar{P}(x) = \nu P(x)$; hence, $\bar{c}_i = c_i \nu$.

Weight redistribution is performed after model training, specifically immediately following node fusing, and prior to inference. It reduces multiplicative depth, while maintaining model equivalence. Figure 3 illustrates common cases for CNNs, including residual connections, where redistribution must be applied consistently along all converging or diverging branches. Refer to §B.2 for detailed derivations for all cases.

4.3 Tower Reuse

In CKKS, the RNS moduli are typically selected as primes close to the scaling factor Δ . This choice is motivated by the fact that the scaling factors of operands multiply after each homomorphic multiplication, yielding a ciphertext with scale Δ^2 . To prevent exponential growth of the scale, the *rescale* operation is used to reduce the scale back to Δ , consuming one modulus from the modulus chain in the process. For this reason, the number of moduli depends on the application’s multiplicative depth δ . Since homomorphic operations are carried out across all moduli, their number directly impacts computational efficiency. Rescaling also introduces approximation errors: the further the dropped modulus from Δ , the larger the error. This issue is especially relevant for small scaling factors, as fewer RNS primes lie relatively close to Δ . These errors can accumulate and amplify through subsequent homomorphic operations, increasing the likelihood of incorrect results. Using a large Δ has drawbacks, as it requires larger RNS moduli and therefore increases the ciphertext modulus $Q = \prod_{i=0}^{\mathcal{L}} q_i$, where \mathcal{L} is the number of levels and q_i are the RNS primes, which reduces the security level. One can increase security by increasing the polynomial degree N . However, it is undesirable because operating on larger polynomials slows computation. Thus, for a fixed security level and polynomial degree, there is a maximum allowable Q . Consequently, for an application-defined δ , this imposes a bound on the maximum Δ . In practice, when δ is large, as is common in deep learning models, the resulting Δ is small.

Proposed Solution. We introduce *tower reuse*, a more general method for determining the RNS moduli by introducing *sublevels* within each level. Instead of enforcing $q_i \approx \Delta$, we allow $q_i \approx \Delta^\ell$, where ℓ denotes the number of sublevels. Rescaling is performed only when a ciphertext scale exceeds the sublevel capacity of the modulus to be dropped. Formally, $\lambda(x) > \lambda(q_i) \implies \downarrow x$, where x represents a ciphertext, \downarrow denotes the rescale operation, and $\lambda(x) = \lfloor \log_\Delta \Delta_x \rfloor$ returns the sublevel of a ciphertext, plaintext, or modulus: with Δ_x referring to the scale of x and Δ being the default scaling factor defined by the encryption parameters.

Example. Suppose following an activation function, there is a convolution. Let modulus $q_i \approx \Delta^2$, thus $\lambda(q_i) = 2$. Consider an input x with scaling factor $\Delta_x = \Delta$, giving $\lambda(x) = 1$. Applying a quadratic activation $y = x^2 + c_1x + c_0$ yields $\lambda(y) = 2$, with $\lambda(c_1) = 1$ and $\lambda(c_0) = 2$. Next, a convolution $z = \sum_i \omega_i y_i + \alpha$ is performed. Since $\lambda(y) = 2$, by setting $\lambda(\omega) = 1$, we obtain $\lambda(z) = 3$. As $\lambda(z) > \lambda(q_i)$, a rescale is triggered. The rescale operation drops q_i from the modulus chain, reducing the level $\Lambda(\cdot)$ by one and resetting the sublevel to one:

$$\Lambda(\downarrow z) = \Lambda(z) - 1, \quad \lambda(\downarrow z) = \lambda(z) - \lambda(q_i) = 1.$$

In terms of Δ , a ciphertext z with $\Delta_z = \Delta^3$ rescaled by $q_i \approx \Delta^2$ results in output scale $\Delta_{\downarrow z} \approx \Delta$.

Tower reuse is an automatic inference-time technique governed by q_i , Δ , and the network structure. It improves computational efficiency and reduces approximation errors. The efficiency gains arise from decreasing the number of RNS moduli by a factor of ℓ , since the method allows ℓ levels of multiplication to be performed before rescaling, and from the corresponding reduction in the number of required rescale operations. The reduction in approximation error is likewise due to the fewer rescale operations, and also to the fact that the method permits the use of smaller Δ values together with larger q_i , making the moduli relatively closer to Δ^ℓ .

4.4 Impact on RNS Levels

The combination of our polynomial activation function with the structural optimizations proposed in this section reduces the number of RNS levels \mathcal{L} required for multiplication compared to PILLAR [11], which previously achieved the lowest \mathcal{L} : from 79 to 16 for VGG-16, 87 to 18 for ResNet-18, 97 to 20 for ResNet-20, and 157 to 32 for ResNet-32.

Level Analysis. Table 1 summarizes the number of levels \mathcal{L} required for multiplication across VGG and ResNet models under various optimization techniques. To illustrate, we focus on ResNet-18, which comprises 17 convolutional layers, batch normalization layers, and activation functions, along with a single average pooling and linear layer:

- P_4 . Prior work with the lowest \mathcal{L} [11] uses a degree-4 polynomial activation, giving $\mathcal{L} = 87$: convolutions, batch normalizations, average pooling, and linear layers each contribute $\mathcal{L} = 1$, and the activation contributes $\mathcal{L} = 3$.
- P_2 . By replacing the activation function with a degree-2 polynomial, as described in §3, the required level for activations drops to 2, reducing the model \mathcal{L} to 70.
- P_2F . Employing node fusing (§4.1) on P_2 removes all batch normalizations, which lowers \mathcal{L} to 53.
- P_2R . Applying weight redistribution (§4.2) to P_2 instead yields $\mathcal{L} = 35$. The highest-order coefficients in batch normalizations and polynomial activations are normalized to one, simplifying them to $x + b_0$ ($\mathcal{L} = 0$) and $x^2 + c_1x + c_0$ ($\mathcal{L} = 1$); the average-pooling divisor is likewise normalized to one ($\mathcal{L} = 0$). These simplifications give $\mathcal{L} = 35$.
- P_2FR . Combining node fusing and weight redistribution retains $\mathcal{L} = 35$, but reduces homomorphic operations, since node fusing eliminates batch normalizations.
- P_2FRT . Applying tower reuse (§4.3) to P_2FR lets a non-linear polynomial activation and subsequent linear kernel share a level, halving the number of levels to $\mathcal{L} = 18$, following $\mathcal{L}_{P_2FRT} = \lceil \frac{\mathcal{L}_{P_2FR}}{2} \rceil$ for VGG and ResNet models.

In summary, by combining a lower-degree polynomial activation with structural optimizations, we reduce levels by nearly a factor of five compared to prior work.

Table 1: Number of RNS levels required for homomorphic multiplications in VGG and ResNet models. P_4 : Degree-4 polynomial activation used in PILLAR [11]. P_2 : Degree-2 polynomial activation (§3). P_2F : P_2 with node fusing (§4.1). P_2R : P_2 with weight redistribution (§4.2). P_2FR : P_2 with node fusing and weight redistribution. P_2FRT : P_2FR with tower reuse (§4.3).

Model	P_4	P_2	P_2F	P_2R	P_2FR	P_2FRT
VGG-16	79	64	51	31	31	16
ResNet-18	87	70	53	35	35	18
ResNet-20	97	78	59	39	39	20
ResNet-32	157	126	95	63	63	32

5 Co-design Techniques

5.1 Data Layout

Data layout defines how model inputs and weights are mapped into FHE ciphertext and plaintext slots during encoding. In this work, we adopt the *HW layout* [9], which assigns each input channel to a separate ciphertext and fills its slots with spatial values indexed by two-dimensional coordinates. Unlike the naive layout [13], where each ciphertext holds only one value and incurs significant overhead, HW layout is more efficient, packing $h \cdot w$ values per ciphertext, with h and w denoting input height and width. Figure 4 shows this for a $3 \times 4 \times 4$ input with a $3 \times 2 \times 2$ filters (stride 1, no padding), illustrating slot arrangements and gaps that may appear after convolution or other kernel operations. These gaps could be removed by remapping, but that requires additional multiplications and increases multiplicative depth. Instead, we use an *adaptive (lazy) mapping* strategy: some slots are left unused, and subsequent weights, biases, and coefficients are aligned with the slot arrangement of the preceding layer’s output. HW layout does not always fully utilize slots, especially when input channels have far fewer values than available slots. More compact layouts such as *CHW layout* [9] and its variants [20] address this by mapping multiple channels into one ciphertext, which reduces ciphertext counts and decreases the number of multiplications and additions, ultimately leading to faster inference. However, PPML relies on polynomial approximations that reduce accuracy compared to plaintext ReLU models. For this reason, we retain the less efficient HW layout, repurposing unused slots to improve accuracy instead of minimizing inference time. To offset the added latency, we introduce a parameter clustering technique.

5.2 Clustering of Convolution Parameters

Convolution layers account for the majority of parameters in deep neural networks, and their handling under FHE is particularly costly. Each convolution weight must be encoded repeatedly to match varying ciphertext layouts and levels, which depend on kernel position and layer structure. As a result, the

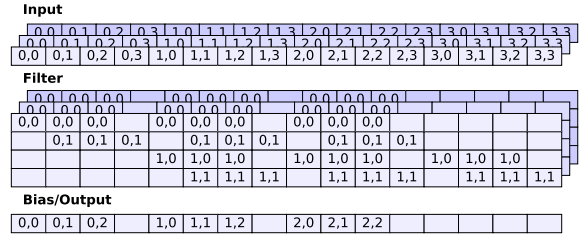


Figure 4: Illustration of HW layout for convolution on a $3 \times 4 \times 4$ input and a $3 \times 2 \times 2$ filter, configured with padding 0 and stride 1.

same scalar weight is often redundantly encoded many times. Pre-encoding all possible weight–layout combinations would lead to prohibitive memory usage, while encoding weights on-demand reduces memory usage but introduces heavy computational cost. To mitigate this overhead, we restrict weights to a small, fixed set of representative values. Each representative is encoded once into a plaintext codebook, and during inference, the appropriate plaintext is retrieved rather than recomputed. Consequently, both runtime and memory scale with the codebook size rather than with the total number of weights. Clustering provides a mechanism for constructing such a representative set by grouping similar weights and replacing each with its nearest *centroid*, thereby bounding the number of unique encodings.

Formally, consider a polynomial network with L convolution layers. The weight tensor of layer l is denoted by $W^{(l)} \in \mathbb{R}^{O_l \times I_l \times H_l \times W_l}$, where O_l is the number of output channels, I_l the number of input channels, and $H_l \times W_l$ the kernel size. Flattening all convolution weights gives $\theta = (\theta_1, \dots, \theta_P) \in \mathbb{R}^P$, where P is the total number of convolution parameters. To compress the model, each θ_j is replaced by its nearest codebook value from $\mathcal{C} = \{c_1, \dots, c_k\} \subset \mathbb{R}$, where $k \ll P$ is the number of representatives in the codebook. The codebook entries act as *centroids* approximating the original weights. The choice of k determines the efficiency-accuracy tradeoff: smaller k reduces the number of encodings but increases approximation error, while larger k produces finer approximation at higher computational and memory cost. Given a distance function $d : \mathbb{R} \times \mathbb{R} \rightarrow \mathbb{R}$ (assumed to be non-negative), each parameter is quantized as: $\tilde{\theta}_j = \arg \min_{c \in \mathcal{C}} d(\theta_j, c)$ for all $j = 1, \dots, P$, producing a quantized parameter vector $\tilde{\theta} \in \mathcal{C}^P$. Quantization is applied elementwise, so each convolutional kernel retains its shape while its values are drawn from the codebook. The choice of clustering strategy determines how the codebook is constructed and how assignments are performed.

Full Clustering. A straightforward strategy is to cluster the entire parameter vector $\theta \in \mathbb{R}^P$ using a single global codebook \mathcal{C} . All convolution parameters, regardless of layer or kernel position, are quantized to the same shared set of representative values. This produces a uniform quantization scheme with simple implementation and a small codebook size.

Limitation. While full clustering reduces the number of distinct weight values, it does not eliminate redundant plaintext encodings. Each weight must still match the ciphertext layout and level of its layer, so the same scalar values appearing in different layers must be re-encoded. Even within a single convolution layer, although all weights share the same level, weights in different filter columns map to different layouts and thus require separate encodings. Only weights in the same column across layer filters align in layout and level. We refer to such a group as a *slice*, which can share plaintext encoding. Thus, full clustering reduces codebook size but fails to address redundancy arising from mismatched levels and layouts.

Slice Clustering. To address the redundancy remaining under full clustering, we refine quantization at the slice level. Since only weights within the same slice can share plaintext encodings, clustering is applied independently to each slice rather than across all parameters. For a given layer l and spatial position $s \in \{1, \dots, W_l\}$, we define the slice $S_s^{(l)} = \{W_{o,i,h,s}^{(l)} | o = 1, \dots, O_l; i = 1, \dots, I_l; h = 1, \dots, H_l\}$, which can be viewed as a vector in $\mathbb{R}^{O_l I_l H_l}$. Each slice $S_s^{(l)}$ is clustered independently using its own codebook $C_s^{(l)} \subset \mathbb{R}$, and quantization is applied elementwise: $\tilde{W}_{o,i,h,s}^{(l)} = \arg \min_{c \in C_s^{(l)}} d(W_{o,i,h,s}^{(l)}, c)$. This ensures clustering respects FHE structure while adapting to the local weight distribution of each slice. Figure 5 illustrates slice clustering for a single convolution layer. Convolution filters are decomposed into vertical slices along the kernel width dimension W_l . Each colored slice $S_s^{(l)}$ is clustered independently using its own codebook. Each three-dimensional block represents a convolution filter associated with one output channel. The three axes correspond to kernel height H_l (vertical), kernel width W_l (horizontal), and input channels I_l (depth). The collection of such filters forms the output channels O_l . Slices are taken as vertical strips along the width dimension W_l , and the figure highlights them with distinct colors. The blue strip corresponds to slice $S_1^{(l)}$, the yellow strip to slice $S_2^{(l)}$, and the pink strip to slice $S_3^{(l)}$. Each slice $S_s^{(l)}$ groups together all weights $W_{o,i,h,s}^{(l)}$ at a fixed width position s across output channels O_l , input channels I_l , and kernel height H_l , and is clustered independently with its own codebook $C_s^{(l)}$. This illustration emphasizes that clustering is performed slice by slice, rather than across the entire filter volume.

5.3 Ensemble of Polynomial Network

Inference with a single polynomial network $g(x)$ often shows high variance across training runs. Let $g_{(m)}(x) \in \mathbb{R}^K$ denote the logits by the m -th independently trained instance. For a fixed input, these logits can differ significantly, especially near decision boundaries, due to (1) approximation error introduced by the fixed-point polynomial activation $p_d(\cdot)$ and (2) training stochasticity such as random weight initialization and mini-batch ordering. As a result, different $g_{(m)}$ in-

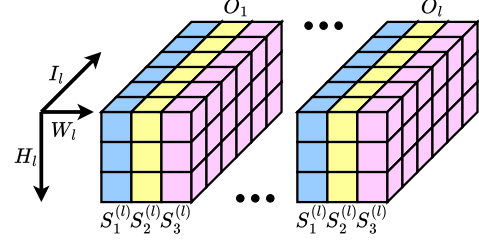


Figure 5: Illustration of single model slice clustering. Convolution filters are decomposed into slices along the kernel width, and each slice is clustered independently with its own codebook.

stances may predict different classes for the same input. To reduce this variance, we use an ensemble of M polynomial networks $\{g_{(m)}\}_{m=1}^M$. All ensemble members share the same architecture and activation $p_d(\cdot)$, but are trained independently with different random seeds and mini-batch orders. Given an input x , the ensemble output is defined as the average of logits: $\bar{g}(x) = \frac{1}{M} \sum_{m=1}^M g_{(m)}(x)$ with the predicted class $\hat{y} = \arg \max_{k \in \{1, \dots, K\}} \bar{g}(x)_k$. Logit averaging smooths both training noise and polynomial approximation errors, producing more stable and accurate predictions. Each $g_{(m)}$ is trained using the same regularized loss \mathcal{L}_B (Eq. 1), ensuring compatibility with fixed-point polynomial inference under FHE. Crucially, this ensemble design adds no additional computation or memory overhead. As described in §5.1, our HW layout leaves a subset of ciphertext slots unused. We populate these slots with weights from different ensemble members, while all models share the same ciphertexts for inputs and activations. This reuse of ciphertext–plaintext structures avoids redundant ciphertexts and repeated encodings, making ensemble inference practical within the FHE framework.

Limits of Ensemble with Clustering. While ensemble inference reuses unused ciphertext slots, naively combining it with parameter clustering introduces a challenge. In slice clustering, each slice $S_s^{(l)}$ containing $O_l \times I_l \times H_l$ weights is represented by k centroids in codebook $C_s^{(l)}$, reducing the number of plaintext encodings to k per slice. In an ensemble setting, however, each plaintext must encode parameters from all M models. Since centroids are unlikely to align across independently trained models, the number of distinct encodings per slice grows as $O(k^M)$, negating the benefits of clustering and making the naive combination impractical.

Slice Ensemble Clustering. To address the inefficiency of independent clustering, we extend slice clustering to ensemble models by enforcing a shared set of representatives across all ensemble members. Specifically, we cluster weights jointly at the same kernel position so that all models use a common codebook. Consider an ensemble of M polynomial networks. For convolutional layer l , model m has weights $W^{(l,m)} \in \mathbb{R}^{O_l \times I_l \times H_l \times W_l}$. For each kernel width position $s \in \{1, \dots, W_l\}$, we extract slices: $S_s^{(l,m)} = \{W_{o,i,h,s}^{(l,m)} | o =$

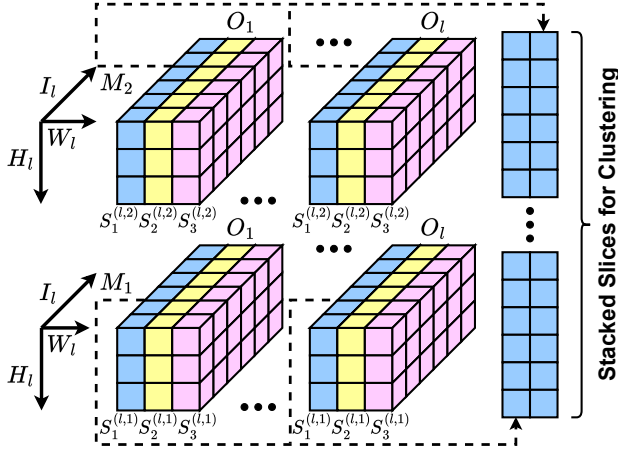


Figure 6: Illustration of slice-wise clustering for an ensemble. Slices at the same kernel width position from different models are stacked and clustered jointly using a shared codebook.

$1, \dots, O_i; i = 1, \dots, I_l; h = 1, \dots, H_l$. Stacking slices from all M models produces $X_s^{(l)} = [S_s^{(l,1)} S_s^{(l,2)} \dots S_s^{(l,M)}] \in \mathbb{R}^{N_s \times M}$, where $N_s = O_i I_l H_l$. Each row of $X_s^{(l)}$ is an M -dimensional vector corresponding to the same weight coordinate across all models. We cluster these rows in \mathbb{R}^M by solving: $\min_{C_s^{(l)} \subset \mathbb{R}^M} \sum_{j=1}^{N_s} \min_{c \in C_s^{(l)}} d(X_{s,j}^{(l)}, c)$, where $C_s^{(l)} = \{c_1, \dots, c_k\}$ is the shared codebook. Each row $X_{s,j}^{(l)}$ is replaced by its nearest centroid, producing quantized slices $\tilde{X}_{s,j}^{(l)} \in C_s^{(l)}$. Quantized weights $\tilde{W}^{(l,m)}$ are then reconstructed by reshaping the corresponding slices. This shared clustering aligns weights across ensemble members, mapping small per-model variations at the same coordinate to a common centroid. It thus requires fewer distinct encodings, reducing codebook size and inference time while retaining the accuracy gains of ensembling. Figure 6 illustrates how slice clustering is extended from a single model to an ensemble of polynomial networks. Each three-dimensional block in the figure represents the convolution filters of a single model instance, spanning kernel height H_l , kernel width W_l , and input channels I_l . The collection of such filters across output channels O_l forms the layer weights $W^{(l,m)}$ for model m . For a fixed layer l , slices are extracted as vertical strips along the width dimension W_l , with colors indicating different slices $S_s^{(l,m)}$ within each model. Unlike the single-model case, however, we now align slices from multiple models at the same width position s and stack them together. This produces a slice matrix $X_s^{(l)} \in \mathbb{R}^{N_s \times M}$, where each row corresponds to one weight coordinate across all M models, and $N_s = O_l I_l H_l$. Clustering is then performed jointly in \mathbb{R}^M across models, producing a shared codebook $C_s^{(l)}$ for slice s . The illustration emphasizes that ensemble clustering is not applied to each model independently. Instead, slices are stacked across models at the same spatial position, and clustering is performed jointly.

6 Experimental Results

6.1 Evaluation of Training Methodology

Training Setup. We evaluate our polynomial approximation strategy on the CIFAR-10, CIFAR-100, and Tiny-ImageNet (referred to as Tiny) datasets, which are widely adopted in related work on privacy-preserving neural network inference. Our experiments use ResNet-18, ResNet-20, and ResNet-32 architectures, and additionally include VGG-16 to assess generality beyond residual networks. Each experiment is repeated 10 times with different random seeds, and we report mean classification accuracy along with standard deviations. For model training (see §3), we set the clipping parameter to $c = 2$ and the penalty strength to $\zeta = 0.001$; the impact of both hyperparameters is analyzed subsequently. We fix the fixed-point precision to $b = 10$, following PILLAR [11], as it provides accurate polynomial approximation under quantization-aware fitting. For all clustering strategies, we use the ℓ_2 norm as the distance metric and employ k -means clustering [22].

Impact of Clipping Parameter (c). We evaluate the effect of the clipping interval $[-c, c]$ on model performance. The choice of c determines the trade-off between preserving the activation distribution and truncating extreme values. If c is too small, informative activations are excessively clipped, reducing representational capacity; conversely, if c is too large, the clipping mechanism provides little stabilization, allowing unstable activations to propagate. Results are reported for ResNet-18 on CIFAR-10, which we present without loss of generality. Figure 7a shows the distribution of pre-activation inputs to ReLU across the network. The values are largely concentrated within the interval $[-2, 2]$, with only a small fraction outside this range, supporting the choice of restricting pre-activations to $[-2, 2]$. Figure 7b shows the classification accuracy obtained under different clipping intervals. Among the tested ranges, $[-2, 2]$ consistently achieves the highest mean accuracy across runs. Smaller intervals degraded performance by discarding a substantial portion of activations, while larger intervals reduce stability and result in lower accuracy. This trend is consistent across other dataset–architecture combinations. Based on these observations, we adopt $[-2, 2]$ as the clipping range in all experiments.

Impact of Penalty Strength (ζ). We analyze the impact of the penalty strength ζ on model performance. The parameter ζ controls the magnitude of the regularization term that penalizes pre-activations outside the target interval $[-c, c]$. Figure 7c reports results ResNet-18 on CIFAR-10. The highest mean accuracy is obtained for $\zeta = 10^{-3}$. Smaller values fail to provide sufficient regularization and lead to degraded accuracy, whereas larger values reduce performance by overly constraining the model. This trend is consistent across other dataset–architecture combinations. Based on these observations, we set $\zeta = 10^{-3}$ in all experiments.

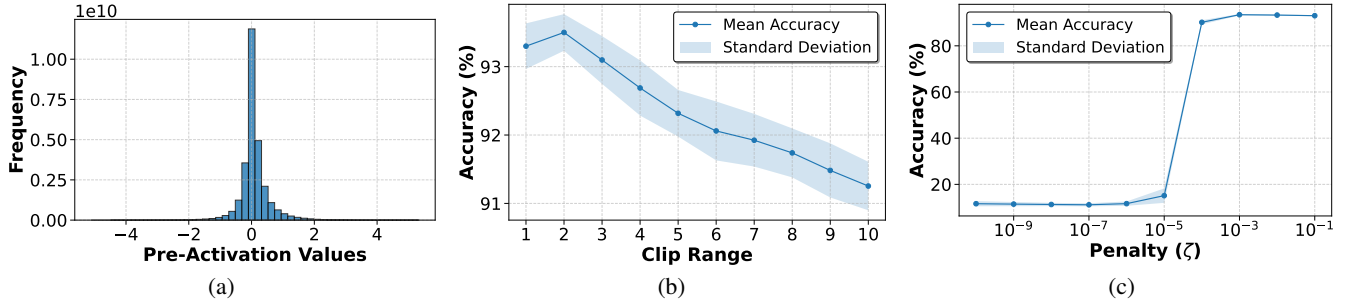


Figure 7: Effects of activation clipping and regularization for ResNet-18 on CIFAR-10. (a) Pre-Activation value distribution across all layers, showing concentration within $[-2, 2]$. (b) Accuracy across clipping ranges, with $[-2, 2]$ performing best. (c) Accuracy versus penalty strength ζ , with best performance at $\zeta = 10^{-3}$; smaller values under-regularize the model, while larger values overly constrain it and reduce accuracy.

Comparison to Related Work. We compare the training methodology of our approach against PILLAR, which represents the lowest-degree polynomial-approximation method previously shown to train deep neural networks reliably. We evaluate PILLAR using its open-source implementation [3]. PILLAR was originally designed in the context of interactive PPML, which differs from our non-interactive setting, and its repository does not provide any implementation for private inference. For these reasons, we restrict the comparison to classification accuracy and do not evaluate inference time. Table 2 reports classification accuracies (mean \pm standard deviation) across all evaluated datasets and architectures using ReLU, PAPER (our method), and two versions of PILLAR. The original PILLAR method employs a degree-4 polynomial activation. For a fair comparison, we additionally adapt this implementation to use a degree-2 polynomial, allowing a direct comparison with PAPER at the same polynomial degree while keeping the original training procedure unchanged. As shown in Table 2, when averaged across all datasets and architectures, the adapted degree-2 variant of PILLAR exhibits a substantial degradation in accuracy, with an average drop of 7.99% relative to ReLU and notably high variance, particularly on more challenging datasets such as CIFAR-100 and Tiny-ImageNet. The original degree-4 variant of PILLAR is more stable but still underperforms ReLU, with an average accuracy gap of 6.54%. In contrast, PAPER with degree-2 polynomial activation remains much closer to ReLU, incurring an average accuracy drop of only 1.84% across all datasets and architectures. Importantly, PAPER demonstrates consistently stable training behavior across all evaluated settings, avoiding the large run-to-run fluctuations seen in both variants of PILLAR. These results demonstrate that while PILLAR either degrades significantly when reduced to a degree-2 configuration or remains less accurate in its intended degree-4 configuration, PAPER enables accurate and stable training with quadratic polynomial activations. Overall, these results indicate that the accuracy gap typically associated with low-degree polynomial approximations arises primarily from limitations in training methodology, and can be substantially mitigated through the regularization techniques introduced in PAPER.

Table 2: Classification accuracy (% , mean \pm standard deviation) on CIFAR and Tiny-ImageNet datasets for VGG and ResNet models using ReLU, PAPER (degree-2), and two versions of PILLAR.

Method	VGG-16	ResNet-18	ResNet-20	ResNet-32
	CIFAR-10			
ReLU	92.57 \pm 0.36	94.57 \pm 0.23	94.84 \pm 0.25	95.23 \pm 0.30
PAPER	90.41 \pm 0.46	93.73 \pm 0.27	94.06 \pm 0.26	93.86 \pm 0.24
PILLAR ($d = 2$)	88.32 \pm 0.19	91.78 \pm 0.13	90.43 \pm 0.40	90.40 \pm 1.73
PILLAR ($d = 4$)	90.76 \pm 0.18	93.26 \pm 0.15	90.98 \pm 0.29	92.24 \pm 0.27

Method	ResNet-18	ResNet-20	ResNet-32	ResNet-32
	CIFAR-100			Tiny
ReLU	76.22 \pm 0.44	74.96 \pm 0.36	76.58 \pm 0.40	61.37 \pm 0.36
PAPER	74.96 \pm 0.51	73.89 \pm 0.37	73.93 \pm 0.53	56.78 \pm 0.42
PILLAR ($d = 2$)	71.92 \pm 0.28	62.30 \pm 3.96	66.38 \pm 1.78	40.85 \pm 0.68
PILLAR ($d = 4$)	74.81 \pm 0.22	62.55 \pm 7.51	66.10 \pm 1.12	43.29 \pm 0.83

Note: The original PILLAR method uses a degree-4 polynomial [11]; the degree-2 variant is our adaptation of its open-source code for comparison.

6.2 Evaluation of Private Inference

Private Inference Setup. Private inference uses an in-house C++20 framework, built on Microsoft SEAL 4.1 [32] for leveled FHE operations and GMP 6.2.1 for multiprecision arithmetic. The framework includes a tool to automatically convert trained models for C++ inference. All experiments, including related work, were run on a machine with two AMD EPYC 64-core processors, 2 TB memory across 32 DDR4 DIMMs at 2933 MT/s, on Ubuntu 22.04.5 LTS. For PAPER, we set $N = 2^{16}$ for ResNet-32 and $N = 2^{15}$ for the other models, as these are the smallest polynomial degrees enabling correct inference with ≈ 128 -bit security. Details on FHE encryption parameters are in §C. We compare our approach against state-of-the-art non-interactive PPML baselines, MPCNN [20] and AutoFHE [5], in terms of accuracy and inference time, using their publicly available implementations [1, 2] as is. Both baselines implement ResNet-20 on CIFAR-10 and ResNet-32 on CIFAR-10 and CIFAR-100, all with $N = 2^{16}$. We also train plaintext models using standard ReLU activations to serve as reference for accuracy. Figure 8 summarizes private inference time versus accuracy across several CNN models and datasets, comparing clustering methods, ensembles, and baselines.

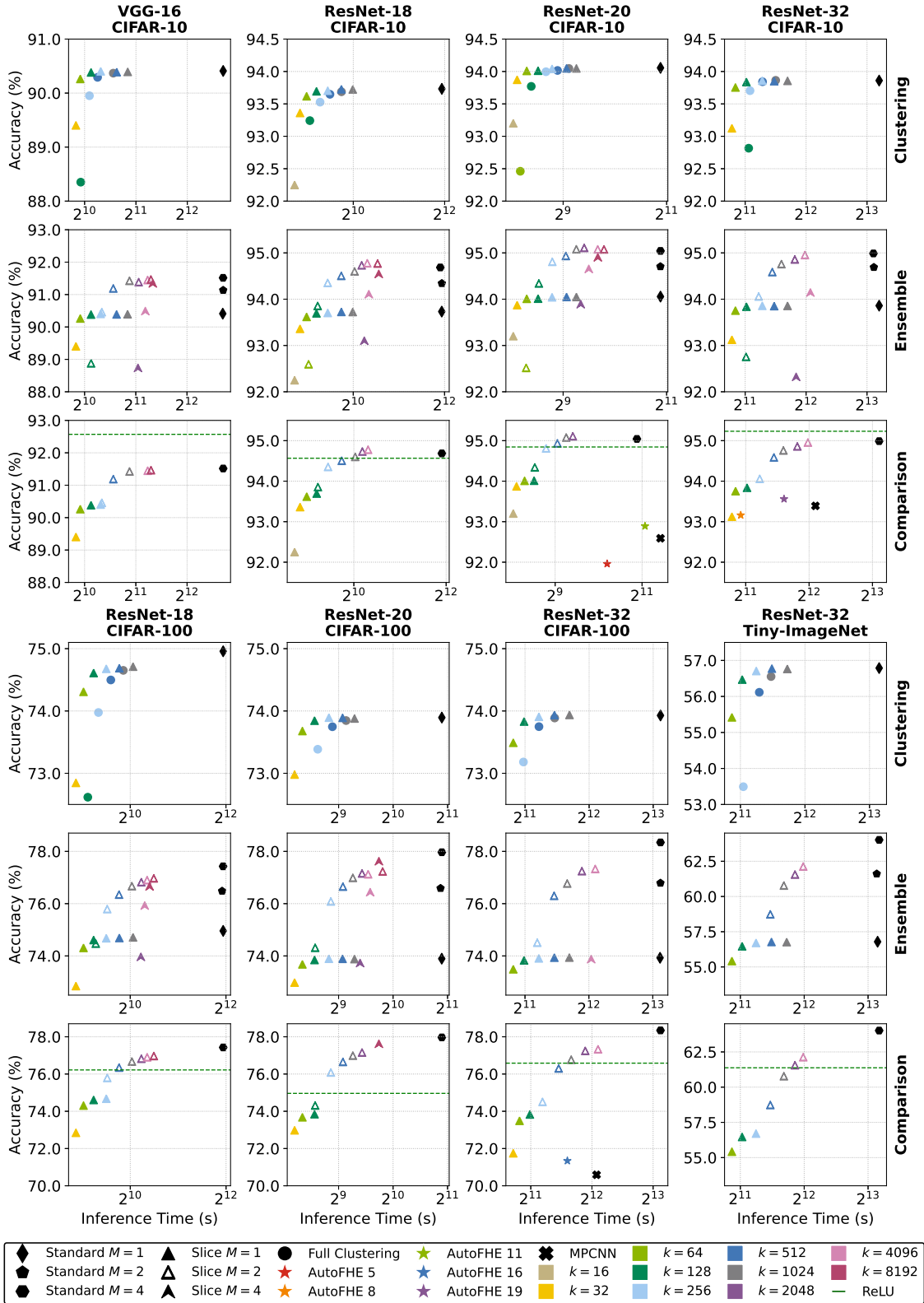


Figure 8: Accuracy vs. private inference time for VGG and ResNet models on CIFAR and Tiny-ImageNet datasets. Ensembles are evaluated with $M \in \{1, 2, 4\}$ ($M = 1$ is a single model). We compare Standard ensembles (no clustering), Slice ensembles (Slice Clustering), and Full Clustering. Colored squares represent centroid counts ($k = 16, \dots, 8192$), and the same color is used for the same centroid count in both slice and full clustering. Baselines include AutoFHE (numbers = bootstrapping layers) and MPCNN. The green line shows plaintext ReLU accuracy.

Analysis of Parameter Clustering. Figure 8 (rows 1 and 4) shows accuracy and inference time for three configurations: *Standard*, *Full Clustering*, and *Slice Clustering*. *Standard* applies techniques from §3 and §4, while *Full Clustering* and *Slice Clustering* extend them with parameter clustering described in §5.2. Clustering reduces inference time several-fold compared to *Standard*, while maintaining similar accuracy. At very low centroid counts (k), accuracy degrades due to insufficient parameter representation. Beyond a threshold (e.g., $k = 64$ for *Slice Clustering*), accuracy matches *Standard* while providing 4-7 \times speedups. For a fixed k , *Full Clustering* is slightly faster, as its centroids are shared across slices and convolutional layers and thus are not fully utilized within individual slices. By contrast, *Slice Clustering* employs all centroids within each slice, incurring additional computational overhead from extra plaintext encoding, but providing finer granularity and improved parameter representation, resulting in higher accuracy. In fact, *Slice Clustering* with $k = 32$ achieves higher accuracy and faster inference than *Full Clustering* with $k = 64$. Overall, *Slice Clustering* is superior, surpassing *Full Clustering* in both accuracy and latency.

Ensemble Evaluation. In Figure 8 (rows 2 and 5), we evaluate ensembles with $M = \{1, 2, 4\}$ models. The figure depicts accuracy and inference time for two approaches: *Standard-M* (ensembles without clustering) and *Slice-M* (ensembles with slice clustering as in §5.3). Inference time does not increase with ensemble size since all models fit in one ciphertext, requiring the same number of homomorphic operations. For *Standard-M*, accuracy consistently improves as M increases. *Slice-M*, however, does not always scale the same way. Since each centroid represents an M -dimensional space, higher M can require more centroids to capture model parameters. Thus, *Slice-4* can underperform *Slice-2* at a fixed k , and *Slice-2* needs more centroids to match *Standard-2* accuracy than either method with $M = 1$. Despite this, *Slice-M* is advantageous as it produces models with higher accuracy. For instance, *Slice-2* outperforms *Standard-2* and reaches accuracy comparable to *Standard-4*. This suggests clustering acts as an implicit regularizer that mitigates overfitting.

Accuracy of Polynomial Approximation. Figure 8 (rows 3 and 6) presents Pareto fronts for *Slice Clustering* in terms of accuracy and private inference time, and compares them against AutoFHE and MPCNN. For reference, the figure also reports *Standard-4* and plaintext ReLU accuracy. Beyond the gains obtained from our training methodology, *Slice Ensemble Clustering* (§5.3) further improves accuracy by ensembling multiple models within a single ciphertext. For the simpler CIFAR-10 dataset, *Slice Clustering* achieves accuracy ranging from 1.1% below to 0.3% above ReLU. For the more complex CIFAR-100 and Tiny-ImageNet datasets, our approach consistently surpasses ReLU by 0.7–2.6%. These results demonstrate that our method enables the effective use of low-degree polynomial activations without sacrificing accuracy.

Comparison to Related Work. For ResNet-20, where our models operate with $N = 2^{15}$, *Slice Clustering* achieves consistently faster inference than related work (up to 4 \times). For ResNet-32, where all approaches use $N = 2^{16}$, our method is comparable in inference time to AutoFHE on CIFAR-10 and 2 \times faster on CIFAR-100. Inference time does not change for our approach for different datasets, whereas AutoFHE slows down because it requires a high number of bootstrapping operations to maintain accuracy. The main factors affecting our inference time relative to related work are: (i) the polynomial activation (§3) and structural optimizations (§4) reduce both multiplicative depth and number of RNS moduli, allowing execution under LFHE without bootstrapping; (ii) our clustering technique (§5.2) further reduces the number of unique parameters, thereby limiting plaintext encodings per convolution; (iii) for ResNet-20, we operate at a smaller polynomial degree, which directly accelerates homomorphic operations; (iv) our choice of data layout (§5.1) deliberately sacrifices some latency to better exploit ciphertext slots for accuracy, but the above optimizations offset this overhead. In terms of accuracy, our approach consistently outperforms related work thanks to our training strategy (§3). In fact, it closely matches plaintext ReLU models, effectively eliminating the accuracy gap typically observed in polynomial approximations of CNNs.

Scalability. The training methodology and optimization techniques exhibit scalability along multiple dimensions: they (i) are applicable to different CNN architectures, as demonstrated with VGG and ResNet models; (ii) extend to deeper networks, allowing more layers before bootstrapping, as shown with ResNet-32, whereas prior LFHE works were limited to AlexNet and VGG-11 [12]; (iii) support datasets with both a small (CIFAR-10) and a large number of classes (CIFAR-100); and (iv) accommodate higher-resolution images (Tiny-ImageNet) with no inference slowdown provided the number of ciphertexts for data encoding remains unchanged.

7 Conclusion

This work advances the practicality of PPML under FHE. We demonstrated that by integrating low-degree polynomial activations with structural and co-design optimizations, it is possible to execute large-scale models such as VGG and ResNet under leveled FHE without bootstrapping, an achievement previously considered not possible. State-of-the-art methods typically incur a 2-5% accuracy loss compared to plaintext models. Our method is the first to close this gap, achieving accuracy on par with ReLU baselines while delivering up to 4 \times faster private inference on CIFAR and Tiny-ImageNet datasets. These results mark an important step toward making PPML deployable in real-world applications, particularly in domains where data confidentiality is non-negotiable. Future research will extend these methods to larger datasets and deeper architectures to further expand the practicality of PPML.

Ethical Considerations

Our work focuses on improving the computational efficiency and accuracy of privacy-preserving machine learning using leveled FHE. All experiments use publicly available benchmark datasets such as CIFAR-10, CIFAR-100, and Tiny-ImageNet. The research does not involve human subjects, personal data, or interactions with live systems. The primary stakeholders are end users who need strong protection for sensitive data, organizations that provide encrypted inference services, and the research community. Our techniques reduce reliance on costly bootstrapping and allow deeper neural networks to run efficiently on encrypted inputs. This provides a clear societal benefit by making practical privacy-preserving machine learning more accessible. The method operates strictly within the security guarantees of the underlying cryptographic scheme and does not introduce new vulnerabilities or mechanisms that could enable data misuse or surveillance. It focuses solely on improving the performance of established secure computation methods. All implementation details and model configurations are included to support reproducibility. Because the research does not involve human subjects, sensitive information, or activities that require institutional oversight, no IRB review is required.

References

- [1] FHE-MP-CNN. <https://github.com/snu-ccl/FHE-MP-CNN>, 2022. Commit hash: a752630.
- [2] AutoFHE: Automated Adaption of CNNs for Efficient Evaluation over FHE. <https://github.com/human-analysis/AutoFHE>, 2024. Commit hash: 984b5b1.
- [3] Fast and Private Inference of Deep Neural Networks by Co-designing Activation Functions. <https://github.com/LucasFenaux/PILLAR-ESPN>, 2024. Commit hash: b3522ca.
- [4] Syed Muhammad Anwar, Muhammad Majid, Adnan Qayyum, Muhammad Awais, Majdi R. Alnowami, and Muhammad Khurram Khan. Medical Image Analysis using Convolutional Neural Networks: A Review. *Journal of Medical Systems*, 42(11):226, 2018.
- [5] Wei Ao and Vishnu Naresh Boddeti. AutoFHE: Automated Adaption of CNNs for Efficient Evaluation over FHE. In *33rd USENIX Security Symposium, USENIX Security 2024, Philadelphia, PA, USA, August 14-16, 2024*. USENIX Association, 2024.
- [6] Alon Brutzkus, Ran Gilad-Bachrach, and Oren Elisha. Low Latency Privacy Preserving Inference. In *Proceedings of the 36th International Conference on Machine Learning, ICML 2019, 9-15 June 2019, Long Beach, California, USA*, volume 97 of *Proceedings of Machine Learning Research*, pages 812–821. PMLR, 2019.
- [7] Jung Hee Cheon, Kyoohyung Han, Andrey Kim, Miran Kim, and Yongsoo Song. A Full RNS Variant of Approximate Homomorphic Encryption. In *Selected Areas in Cryptography - SAC 2018 - 25th International Conference, Calgary, AB, Canada, August 15-17, 2018, Revised Selected Papers*, volume 11349 of *Lecture Notes in Computer Science*, pages 347–368. Springer, 2018.
- [8] Jung Hee Cheon, Andrey Kim, Miran Kim, and Yong Soo Song. Homomorphic Encryption for Arithmetic of Approximate Numbers. In *Advances in Cryptology - ASIACRYPT 2017 - 23rd International Conference on the Theory and Applications of Cryptology and Information Security, Hong Kong, China, December 3-7, 2017, Proceedings, Part I*, volume 10624 of *Lecture Notes in Computer Science*, pages 409–437. Springer, 2017.
- [9] Roshan Dathathri, Olli Saarikivi, Hao Chen, Kim Laine, Kristin E. Lauter, Saeed Maleki, Madanlal Musuvathi, and Todd Mytkowicz. CHET: an optimizing compiler for fully-homomorphic neural-network inferencing. In *Proceedings of the 40th ACM SIGPLAN Conference on Programming Language Design and Implementation, PLDI 2019, Phoenix, AZ, USA, June 22-26, 2019*, pages 142–156. ACM, 2019.
- [10] Jia Deng, Wei Dong, Richard Socher, Li-Jia Li, Kai Li, and Li Fei-Fei. ImageNet: A large-scale hierarchical image database. In *2009 IEEE Computer Society Conference on Computer Vision and Pattern Recognition (CVPR 2009), 20-25 June 2009, Miami, Florida, USA*, pages 248–255. IEEE Computer Society, 2009.
- [11] Abdulrahman Daa, Lucas Fenaux, Thomas Humphries, Marian Dietz, Faezeh Ebrahimiaghazani, Bailey Kacsmar, Xinda Li, Nils Lukas, Rasoul Akhavan Mahdavi, Simon Oya, Ehsan Amjadian, and Florian Kerschbaum. Fast and Private Inference of Deep Neural Networks by Co-designing Activation Functions. In *33rd USENIX Security Symposium, USENIX Security 2024, Philadelphia, PA, USA, August 14-16, 2024*. USENIX Association, 2024.
- [12] Karthik Garimella, Nandan Kumar Jha, and Brandon Reagen. Sisyphus: A Cautionary Tale of Using Low-Degree Polynomial Activations in Privacy-Preserving Deep Learning. *CoRR*, abs/2107.12342, 2021.
- [13] Ran Gilad-Bachrach, Nathan Dowlan, Kim Laine, Kristin E. Lauter, Michael Naehrig, and John Wernsing. CryptoNets: Applying Neural Networks to Encrypted Data with High Throughput and Accuracy. In *Proceedings of the 33rd International Conference on Machine Learning, ICML 2015, June 7-13, 2015, Lake Tahoe, California, USA*, volume 37 of *Proceedings of Machine Learning Research*, pages 1273–1282. PMLR, 2015.

- Learning, ICML 2016, New York City, NY, USA, June 19-24, 2016*, volume 48 of *JMLR Workshop and Conference Proceedings*, pages 201–210. JMLR.org, 2016.
- [14] Zhicong Huang, Wen-jie Lu, Cheng Hong, and Jian-sheng Ding. Cheetah: Lean and Fast Secure Two-Party Deep Neural Network Inference. In *31st USENIX Security Symposium, USENIX Security 2022, Boston, MA, USA, August 10-12, 2022*, pages 809–826. USENIX Association, 2022.
- [15] Siam Umar Hussain, Mojan Javaheripi, Mohammad Samragh, and Farinaz Koushanfar. COINN: Crypto/ML Codesign for Oblivious Inference via Neural Networks. In *CCS '21: 2021 ACM SIGSAC Conference on Computer and Communications Security, Virtual Event, Republic of Korea, November 15 - 19, 2021*, pages 3266–3281. ACM, 2021.
- [16] Chiraag Juvekar, Vinod Vaikuntanathan, and Anantha P. Chandrakasan. GAZELLE: A Low Latency Framework for Secure Neural Network Inference. In *27th USENIX Security Symposium, USENIX Security 2018, Baltimore, MD, USA, August 15-17, 2018*, pages 1651–1669. USENIX Association, 2018.
- [17] Alex Krizhevsky and Geoffrey Hinton. Learning Multiple Layers of Features from Tiny Images. Technical report, University of Toronto, 2009.
- [18] Alex Krizhevsky, Ilya Sutskever, and Geoffrey E. Hinton. ImageNet Classification with Deep Convolutional Neural Networks. In *Advances in Neural Information Processing Systems 25: 26th Annual Conference on Neural Information Processing Systems 2012. Proceedings of a meeting held December 3-6, 2012, Lake Tahoe, Nevada, United States*, pages 1106–1114, 2012.
- [19] Yann LeCun, Léon Bottou, Yoshua Bengio, and Patrick Haffner. Gradient-based learning applied to document recognition. *Proceedings of the IEEE*, 86(11):2278–2324, 1998.
- [20] Eunsang Lee, Joon-Woo Lee, Junghyun Lee, Young-Sik Kim, Yongjune Kim, Jong-Seon No, and Woosuk Choi. Low-Complexity Deep Convolutional Neural Networks on Fully Homomorphic Encryption Using Multiplexed Parallel Convolutions. In *International Conference on Machine Learning, ICML 2022, 17-23 July 2022, Baltimore, Maryland, USA*, volume 162 of *Proceedings of Machine Learning Research*, pages 12403–12422. PMLR, 2022.
- [21] Jian Liu, Mika Juuti, Yao Lu, and N. Asokan. Oblivious Neural Network Predictions via MiniONN Transformations. In *Proceedings of the 2017 ACM SIGSAC Conference on Computer and Communications Security, CCS 2017, Dallas, TX, USA, October 30 - November 03, 2017*, pages 619–631. ACM, 2017.
- [22] Stuart P. Lloyd. Least squares quantization in PCM. *IEEE Transactions on Information Theory*, 28(2):129–136, 1982.
- [23] Qian Lou and Lei Jiang. HEMET: A Homomorphic-Encryption-Friendly Privacy-Preserving Mobile Neural Network Architecture. In *Proceedings of the 38th International Conference on Machine Learning, ICML 2021, 18-24 July 2021, Virtual Event*, volume 139 of *Proceedings of Machine Learning Research*, pages 7102–7110. PMLR, 2021.
- [24] Qian Lou, Yilin Shen, Hongxia Jin, and Lei Jiang. SAFENet: A Secure, Accurate and Fast Neural Network Inference. In *9th International Conference on Learning Representations, ICLR 2021, Virtual Event, Austria, May 3-7, 2021*. OpenReview.net, 2021.
- [25] Vadim Lyubashevsky, Chris Peikert, and Oded Regev. On Ideal Lattices and Learning with Errors over Rings. *Journal of the ACM*, 60(6):43:1–43:35, 2013.
- [26] Nenad Markuš. Fusing batch normalization and convolution in runtime. <https://nenadmarkus.com/p/fusing-batchnorm-and-conv/>, 2018.
- [27] Pratyush Mishra, Ryan Lehmkuhl, Akshayaram Srinivasan, Wenting Zheng, and Raluca Ada Popa. Delphi: A Cryptographic Inference Service for Neural Networks. In *29th USENIX Security Symposium, USENIX Security 2020, August 12-14, 2020*, pages 2505–2522. USENIX Association, 2020.
- [28] Ahmet Murat Özbayoglu, Mehmet Ugur Gudelek, and Omer Berat Sezer. Deep learning for financial applications : A survey. *Applied Soft Computing*, 93:106384, 2020.
- [29] Robert Podschwadt, Daniel Takabi, Peizhao Hu, Mohammad Hossein Rafiei, and Zhipeng Cai. A Survey of Deep Learning Architectures for Privacy-Preserving Machine Learning With Fully Homomorphic Encryption. *IEEE Access*, 10:117477–117500, 2022.
- [30] Mauro Ribeiro, Katarina Grolinger, and Miriam A. M. Capretz. MLaaS: Machine Learning as a Service. In *14th IEEE International Conference on Machine Learning and Applications, ICMLA 2015, Miami, FL, USA, December 9-11, 2015*, pages 896–902. IEEE, 2015.
- [31] Esha Sarkar, Eduardo Chielle, Gamze Gursoy, Leo Chen, Mark Gerstein, and Michail Maniatakos. Privacy-preserving cancer type prediction with homomorphic encryption. *Scientific reports*, 13(1):1661, 2023.

- [32] Microsoft SEAL (release 4.1). <https://github.com/Microsoft/SEAL>, January 2023. Microsoft Research, Redmond, WA.
- [33] Karen Simonyan and Andrew Zisserman. Very Deep Convolutional Networks for Large-Scale Image Recognition. In *3rd International Conference on Learning Representations, ICLR 2015, San Diego, CA, USA, May 7-9, 2015, Conference Track Proceedings*, 2015.
- [34] Ian Zhou, Farzad Tofgh, Massimo Piccardi, Mehran Abolhasan, Daniel Robert Franklin, and Justin Lipman. Secure Multi-Party Computation for Machine Learning: A Survey. *IEEE Access*, 12:53881–53899, 2024.

A Why the Penalty Function Works?

Lemma 1 (Pre-activation Update Decomposition). Let $z_p^{(l)} = W^{(l)} h_{p_d}^{(l-1)}(x) \in \mathbb{R}^{n_l}$ denote the pre-activation vector at layer l for input x . We define two quantities based on this vector: the clipping residual

$$d^{(l)} = z_p^{(l)} - \text{clip}\left(z_p^{(l)}; [-c, c]\right)$$

which measures the amount by which $z_p^{(l)}$ exceeds the clipping range, and the gradient of the cross-entropy loss with respect to the pre-activation

$$g^{(l)} = \frac{\partial}{\partial z_p^{(l)}} \ell_{\text{CE}}(g(x), y)$$

which captures the sensitivity of the loss to changes in $z_p^{(l)}$. After a single gradient-descent update with learning rate η on the minibatch loss \mathcal{L}_B , the change in $z_p^{(l)}$ decomposes as

$$\Delta z_p^{(l)} = \underbrace{(-\eta) \left\| h_{p_d}^{(l-1)}(x) \right\|_2^2 g^{(l)}}_{\Delta z_{\text{CE}}^{(l)}} + \underbrace{(-\eta) \zeta \left\| h_{p_d}^{(l-1)}(x) \right\|_2^2 \frac{d^{(l)}}{\|d^{(l)}\|_2}}_{\Delta z_{\text{pen}}^{(l)}}$$

Here, $\Delta z_{\text{CE}}^{(l)}$ is the component induced by the cross-entropy loss, while $\Delta z_{\text{pen}}^{(l)}$ is the component induced by the clip-range penalty.

Proof. Consider a single training example (x, y) , where x is the input and y the corresponding true label. The total per-sample loss includes two terms:

$$\ell(x) = \ell_{\text{CE}}(g(x), y) + \zeta R\left(z_p^{(l)}\right), \quad R\left(z_p^{(l)}\right) = \left\| d^{(l)} \right\|_2$$

The first term is the standard cross-entropy loss from the network output $g(x)$. The second term is a layer-specific penalty

that acts only on the pre-activations at layer l , penalizing values that fall outside the clipping interval. A gradient-descent step with learning rate η updates the weight matrix by

$$\begin{aligned} \Delta W^{(l)} &= -\eta \frac{\partial}{\partial W^{(l)}} \ell(x) \\ &= -\eta \left(\frac{\partial}{\partial W^{(l)}} \ell_{\text{CE}}(g(x), y) + \zeta \frac{\partial}{\partial W^{(l)}} R\left(z_p^{(l)}\right) \right) \end{aligned}$$

Since $z_p^{(l)}$ depends linearly on the weights, its Jacobian with respect to $W^{(l)}$ is

$$\frac{\partial}{\partial W^{(l)}} z_p^{(l)} = \left[h_{p_d}^{(l-1)}(x) \right]^\top.$$

Using the chain rule, the gradient of the cross-entropy term with respect to the weights becomes

$$\begin{aligned} \frac{\partial}{\partial W^{(l)}} \ell_{\text{CE}}(g(x), y) &= \frac{\partial}{\partial z_p^{(l)}} \ell_{\text{CE}}(g(x), y) \frac{\partial}{\partial W^{(l)}} z_p^{(l)} \\ &= g^{(l)} \left[h_{p_d}^{(l-1)}(x) \right]^\top \end{aligned}$$

The penalty function $R\left(z_p^{(l)}\right) = \left\| d^{(l)} \right\|_2$ is nonzero only when some elements lie outside $[-c, c]$. Its gradient with respect to $z_p^{(l)}$ is

$$\frac{\partial}{\partial z_p^{(l)}} R\left(z_p^{(l)}\right) = \begin{cases} \frac{d^{(l)}}{\|d^{(l)}\|_2} & \text{if } \|d^{(l)}\|_2 > 0, \\ 0 & \text{if } \|d^{(l)}\|_2 = 0. \end{cases}$$

This expression accounts for the case where the clipping has no effect; that is, when $z_p^{(l)} \in [-c, c]$ elementwise, the clipping residual $d^{(l)}$ becomes zero, and the gradient vanishes accordingly. Applying the chain rule again, we compute

$$\begin{aligned} \frac{\partial}{\partial W^{(l)}} R\left(z_p^{(l)}\right) &= \frac{\partial}{\partial z_p^{(l)}} R\left(z_p^{(l)}\right) \frac{\partial}{\partial W^{(l)}} z_p^{(l)} \\ &= \frac{d^{(l)}}{\|d^{(l)}\|_2} \left[h_{p_d}^{(l-1)}(x) \right]^\top \end{aligned}$$

Putting it all together, we obtain the total update for $W^{(l)}$

$$\Delta W^{(l)} = -\eta \left(g^{(l)} + \zeta \frac{d^{(l)}}{\|d^{(l)}\|_2} \right) \left[h_{p_d}^{(l-1)}(x) \right]^\top$$

By definition, the change in pre-activation $z_p^{(l)}$ after one gradient descent step is given by

$$\begin{aligned} \Delta z_p^{(l)} &= \bar{z}_p^{(l)} - z_p^{(l)} = \bar{W}^{(l)} h_{p_d}^{(l-1)}(x) - W^{(l)} h_{p_d}^{(l-1)}(x) \\ &= \left(W^{(l)} + \Delta W^{(l)} \right) h_{p_d}^{(l-1)}(x) - W^{(l)} h_{p_d}^{(l-1)}(x) \\ &= \Delta W^{(l)} h_{p_d}^{(l-1)}(x) \end{aligned}$$

where $\bar{z}_p^{(l)}$ and $\bar{W}^{(l)}$ are updated pre-activations and weight matrix after one gradient-descent step. Substituting the previously derived expression for $\Delta W^{(l)}$

$$\begin{aligned}\Delta z_p^{(l)} &= -\eta \left(g^{(l)} + \zeta \frac{d^{(l)}}{\|d^{(l)}\|_2} \right) \left[h_{p_d}^{(l-1)}(x) \right]^\top h_{p_d}^{(l-1)}(x) \\ &= -\eta \left(g^{(l)} + \zeta \frac{d^{(l)}}{\|d^{(l)}\|_2} \right) \left\| h_{p_d}^{(l-1)}(x) \right\|_2^2 \\ &= \underbrace{(-\eta) \left\| h_{p_d}^{(l-1)}(x) \right\|_2^2}_{\Delta z_{CE}^{(l)}} g^{(l)} + \underbrace{(-\eta) \zeta \left\| h_{p_d}^{(l-1)}(x) \right\|_2^2 \frac{d^{(l)}}{\|d^{(l)}\|_2}}_{\Delta z_{pen}^{(l)}}\end{aligned}$$

we obtain the penalty components $\Delta z_{CE}^{(l)}$ and $\Delta z_{pen}^{(l)}$. \blacksquare

Lemma 2 (Clipping Gradient Pullback). *Let $\Delta z_{pen}^{(l)}$ be the penalty-induced component of the pre-activation update from Lemma 1, and $d^{(l)}$ be the clipping residual. Then the inner product between $\Delta z_{pen}^{(l)}$ and $d^{(l)}$ satisfies*

$$\left\langle \Delta z_{pen}^{(l)}, d^{(l)} \right\rangle = -\eta \zeta \left\| h_{p_d}^{(l-1)}(x) \right\|_2^2 \left\| d^{(l)} \right\|_2 < 0$$

whenever $\left\| d^{(l)} \right\|_2 \neq 0$. Therefore, $\Delta z_{pen}^{(l)}$ “pulls back” each element of $z_p^{(l)}$ lying outside $[-c, c]$ towards the clipping interval.

Proof. The clipping residual $d^{(l)}$ is defined as the difference between the pre-activation $z_p^{(l)}$ and its clipped version. $\Delta z_{pen}^{(l)}$ is the component in $\Delta z_p^{(l)}$ induced by the clip-range penalty. Taking the inner product of $\Delta z_{pen}^{(l)}$ with $d^{(l)}$ gives

$$\begin{aligned}\left\langle \Delta z_{pen}^{(l)}, d^{(l)} \right\rangle &= \left\langle -\eta \zeta \left\| h_{p_d}^{(l-1)}(x) \right\|_2^2 \frac{d^{(l)}}{\|d^{(l)}\|_2}, d^{(l)} \right\rangle \\ &= -\eta \zeta \left\| h_{p_d}^{(l-1)}(x) \right\|_2^2 \left\langle \frac{d^{(l)}}{\|d^{(l)}\|_2}, d^{(l)} \right\rangle \\ &= -\eta \zeta \left\| h_{p_d}^{(l-1)}(x) \right\|_2^2 \frac{1}{\|d^{(l)}\|_2} \left\| d^{(l)} \right\|_2^2 \\ &= -\eta \zeta \left\| h_{p_d}^{(l-1)}(x) \right\|_2^2 \left\| d^{(l)} \right\|_2\end{aligned}$$

Each factor on the right-hand side: η (learning rate), ζ (regularization parameter), $\left\| h_{p_d}^{(l-1)}(x) \right\|_2^2$ (squared norm of the preceding hidden representation) and $\left\| d^{(l)} \right\|_2$ (magnitude of the clipping residual) are strictly positive whenever any pre-activation lies outside $[-c, c]$. Hence the entire product is strictly negative

$$\left\langle \Delta z_{pen}^{(l)}, d^{(l)} \right\rangle < 0$$

A negative inner product implies that $\Delta z_{pen}^{(l)}$ points in the exact opposite direction of the clipping residual $d^{(l)}$. Consequently, every out-of-range component of pre-activation $z_p^{(l)}$ is pulled back towards the clipping boundary, while pre-activation already within $[-c, c]$ experience no change. \blacksquare

B Details on Structural Optimizations

B.1 Derivations of Node Fusing

Batch normalization in linear form is given by

$$B(x) = b_1 x + b_0, \quad b_1 = \frac{\gamma}{\sigma}, \quad b_0 = \beta_b - b_1 \mu.$$

A quadratic activation $P(x)$ serves as a polynomial substitute for ReLU, where $P(x)$ is given by

$$P(x) = c_2 x^2 + c_1 x + c_0.$$

Case 1: $P(B(x)) \mapsto P(x)$. Start with $B(x) = b_1 x + b_0$.

$$\begin{aligned}P(B(x)) &= c_2 (B(x))^2 + c_1 B(x) + c_0 \\ &= c_2 (b_1 x + b_0)^2 + c_1 (b_1 x + b_0) + c_0 \\ &= c_2 (b_1^2 x^2 + 2b_1 b_0 x + b_0^2) + c_1 b_1 x + c_1 b_0 + c_0 \\ &= (c_2 b_1^2) x^2 + (2c_2 b_1 b_0 + c_1 b_1) x + (c_2 b_0^2 + c_1 b_0 + c_0).\end{aligned}$$

Resulting polynomial coefficients

$$p_2 = b_1^2 c_2, \quad p_1 = b_1 (2b_0 c_2 + c_1), \quad p_0 = b_0^2 c_2 + b_0 c_1 + c_0.$$

Case 2: $B(C(x)) \mapsto C(x)$. Consider a convolution $C(x) = \sum_i w_i x_i + \beta_c$. When batch normalization is applied, it can be rewritten as a rescaled convolution with updated weights and bias.

$$\begin{aligned}B(C(x)) &= b_1 C(x) + b_0 \\ &= b_1 \left(\sum_i w_i x_i + \beta_c \right) + b_0 \\ &= \sum_i (b_1 w_i) x_i + (b_1 \beta_c + b_0).\end{aligned}$$

The equivalent convolution $\sum_i \omega_i x_i + \alpha$ uses the following updated parameters

$$\omega_i = b_1 w_i, \quad \alpha = b_1 \beta_c + b_0.$$

Case 3: $P(B_X(x) + B_Y(y)) \mapsto S(x, y)$. Define $B_X(x) = b_{X1} x + b_{X0}$ and $B_Y(y) = b_{Y1} y + b_{Y0}$. Each of these represents a linearized batch normalization applied to one input variable. Let $z = B_X(x) + B_Y(y) = b_{X1} x + b_{Y1} y + (b_{X0} + b_{Y0})$. Applying the activation

$$\begin{aligned}P(z) &= c_2 z^2 + c_1 z + c_0 \\ &= c_2 (b_{X1} x + b_{Y1} y + b_{X0} + b_{Y0})^2 \\ &\quad + c_1 (b_{X1} x + b_{Y1} y + b_{X0} + b_{Y0}) + c_0.\end{aligned}$$

Expanding the square term

$$z^2 = b_{X1}^2 x^2 + b_{Y1}^2 y^2 + 2b_{X1}b_{Y1}xy + 2b_{X1}(b_{X0} + b_{Y0})x + 2b_{Y1}(b_{X0} + b_{Y0})y + (b_{X0} + b_{Y0})^2.$$

Substituting and grouping terms by monomials

$$\begin{aligned} P(z) &= \underbrace{c_2 b_{X1}^2 x^2}_{d_{X2}} + \underbrace{c_2 b_{Y1}^2 y^2}_{d_{Y2}} + \underbrace{2c_2 b_{X1} b_{Y1} xy}_{d_{XY}} \\ &\quad + \underbrace{[b_{X1}(2c_2(b_{X0} + b_{Y0}) + c_1)] x}_{d_X} \\ &\quad + \underbrace{[b_{Y1}(2c_2(b_{X0} + b_{Y0}) + c_1)] y}_{d_Y} \\ &\quad + \underbrace{[c_2(b_{X0} + b_{Y0})^2 + c_1(b_{X0} + b_{Y0}) + c_0]}_{d_0}. \end{aligned}$$

Hence $S(x, y) = d_{X2}x^2 + d_{Y2}y^2 + d_{XY}xy + d_Xx + d_Yy + d_0$ with the coefficients above.

Case 4: $P(B_X(x) + y) \mapsto S(x, y)$. This is the identity short-cut case. Set $B_X(x) = b_{X1}x + b_{X0}$ and define the combined input as $z = B_X(x) + y = b_{X1}x + y + b_{X0}$. Applying the activation

$$P(z) = c_2 z^2 + c_1 z + c_0.$$

Expanding the square term

$$z^2 = b_{X1}^2 x^2 + y^2 + 2b_{X1}xy + 2b_{X1}b_{X0}x + 2b_{X0}y + b_{X0}^2.$$

Substituting and grouping terms by monomials

$$\begin{aligned} P(z) &= \underbrace{c_2 b_{X1}^2 x^2}_{d_{X2}} + \underbrace{c_2 y^2}_{d_{Y2}} + \underbrace{2c_2 b_{X1} xy}_{d_{XY}} + \underbrace{[b_{X1}(2c_2 b_{X0} + c_1)] x}_{d_X} \\ &\quad + \underbrace{[2c_2 b_{X0} + c_1] y}_{d_Y} + \underbrace{[c_2 b_{X0}^2 + c_1 b_{X0} + c_0]}_{d_0}. \end{aligned}$$

Hence $S(x, y) = d_{X2}x^2 + d_{Y2}y^2 + d_{XY}xy + d_Xx + d_Yy + d_0$ with the coefficients above.

B.2 Derivations of Weight Redistribution

B.2.1 Update Forward

Donors. *Average Pooling.* Start with $\mu(x) = k^{-1} \sum_i x_i$ and its normalized form $\bar{\mu}(x) = \sum_i x_i$. We must find \mathfrak{v} such that $\mathfrak{v}\bar{\mu}(x) = \mu(x)$ is valid

$$\begin{aligned} \mathfrak{v}\bar{\mu}(x) &= \mu(x) \\ \mathfrak{v} \sum_i x_i &= k^{-1} \sum_i x_i \\ \mathfrak{v} &= k^{-1}. \end{aligned}$$

Polynomial Functions. Let $P(x) = \sum_{i=0}^d c_i x^i$ and $\bar{P}(x) = x^d + \sum_{i=0}^{d-1} \bar{c}_i x^i$ be a degree- d polynomial and its normalization,

respectively. For $\mathfrak{v}\bar{P}(x) = P(x)$ to hold we have \mathfrak{v} given by

$$\begin{aligned} \mathfrak{v}\bar{P}(x) &= P(x) \\ \mathfrak{v} \left(x^d + \sum_{i=0}^{d-1} \bar{c}_i x^i \right) &= \sum_{i=0}^d c_i x^i \\ \mathfrak{v} x^d &= c_d x^d \\ \mathfrak{v} &= c_d. \end{aligned}$$

The normalized coefficients must satisfy

$$\begin{aligned} \mathfrak{v}\bar{P}(x) &= P(x) \\ \mathfrak{v} \left(x^d + \sum_{i=0}^{d-1} \bar{c}_i x^i \right) &= \sum_{i=0}^d c_i x^i \\ \mathfrak{v} \bar{c}_i x^i &= c_i x^i \\ \bar{c}_i &= c_i \mathfrak{v}^{-1} \quad \forall i \in \{0, \dots, d-1\}. \end{aligned}$$

Bivariate Polynomial. Consider the degree- d bivariate polynomial $S(x, y) = \sum_{i=0}^d \sum_{j=0}^{d-i} c_{ij} x^i y^j$, and let $\bar{S}(x, y) = x^d + \sum_{i=0}^{d-1} \sum_{j=0}^{d-i} \bar{c}_{ij} x^i y^j$ be its normalization on x (normalizing on y is equivalent). As in the univariate case, we require $\mathfrak{v}\bar{S}(x, y) = S(x, y)$. Thus, \mathfrak{v} is determined by

$$\begin{aligned} \mathfrak{v}\bar{S}(x, y) &= S(x, y) \\ \mathfrak{v} \left(x^d + \sum_{i=0}^{d-1} \sum_{j=0}^{d-i} \bar{c}_{ij} x^i y^j \right) &= \sum_{i=0}^d \sum_{j=0}^{d-i} c_{ij} x^i y^j \\ \mathfrak{v} x^d &= c_{d0} x^d \\ \mathfrak{v} &= c_{d0}. \end{aligned}$$

The normalized coefficients are obtained through

$$\begin{aligned} \mathfrak{v}\bar{S}(x, y) &= S(x, y) \\ \mathfrak{v} \left(x^d + \sum_{i=0}^{d-1} \sum_{j=0}^{d-i} \bar{c}_{ij} x^i y^j \right) &= \sum_{i=0}^d \sum_{j=0}^{d-i} c_{ij} x^i y^j \\ \mathfrak{v} \bar{c}_{ij} x^i y^j &= c_{ij} x^i y^j \\ \bar{c}_{ij} &= c_{ij} \mathfrak{v}^{-1} \quad \forall i \in \{0, \dots, d-1\}, \\ &\quad \forall j \in \{0, \dots, d-i\}. \end{aligned}$$

Receivers. *Kernel Functions.* Let $K(x) = \sum_{i \in I} w_i x_i + \beta$ be the original kernel function and $\bar{K}(x) = \sum_{i \in I} \bar{w}_i x_i + \bar{\beta}$ its updated version. To ensure model equivalence, it must hold that $\bar{K}(\mathfrak{v}^{-1}x) = K(x)$. Therefore, the updated parameters are given as follows

$$\begin{aligned} \bar{K}(\mathfrak{v}^{-1}x) &= K(x) \\ \sum_{i \in I} \bar{w}_i \mathfrak{v}^{-1} x_i + \bar{\beta} &= \sum_{i \in I} w_i x_i + \beta \\ \bar{w}_i \mathfrak{v}^{-1} x_i &= w_i x_i \\ \bar{w}_i &= w_i \mathfrak{v} \quad \forall i \in I, \quad \bar{\beta} = \beta. \end{aligned}$$

Polynomial Functions. For a degree- d polynomial receiver $P(x) = \sum_{i=0}^d c_i x^i$, the coefficients of its updated version $\bar{P}(x) = \sum_{i=0}^d \bar{c}_i x^i$ must be chosen such that $\bar{P}(v^{-1}x) = P(x)$ holds

$$\begin{aligned}\bar{P}(v^{-1}x) &= P(x) \\ \sum_{i=0}^d \bar{c}_i (v^{-1}x)^i &= \sum_{i=0}^d c_i x^i \\ \bar{c}_i v^{-i} x^i &= c_i x^i \\ \bar{c}_i &= c_i v^i \quad \forall i \in \{0, \dots, d\}.\end{aligned}$$

Bivariate Polynomial. For a degree- d bivariate polynomial $S(x, y) = \sum_{i=0}^d \sum_{j=0}^{d-i} c_{ij} x^i y^j$ and its updated version $\bar{S}(x, y) = \sum_{i=0}^d \sum_{j=0}^{d-i} \bar{c}_{ij} x^i y^j$, normalizing with respect to x requires that $\bar{S}(v^{-1}x, y) = S(x, y)$. Consequently, the coefficients of $\bar{S}(\cdot)$ are

$$\begin{aligned}\bar{S}(v^{-1}x, y) &= S(x, y) \\ \sum_{i=0}^d \sum_{j=0}^{d-i} \bar{c}_{ij} (v^{-1}x)^i y^j &= \sum_{i=0}^d \sum_{j=0}^{d-i} c_{ij} x^i y^j \\ \bar{c}_{ij} v^{-i} x^i y^j &= c_{ij} x^i y^j \\ \bar{c}_{ij} &= c_{ij} v^i \quad \forall i \in \{0, \dots, d\}, \\ &\quad \forall j \in \{0, \dots, d-i\}.\end{aligned}$$

B.2.2 Update Backward

Donors. Average Pooling. Start with $\mu(x) = k^{-1} \sum_i x_i$ and its normalization $\bar{\mu}(x) = \sum_i x_i$. We must determine v such that $\bar{\mu}(vx) = \mu(x)$ holds

$$\begin{aligned}\bar{\mu}(vx) &= \mu(x) \\ \sum_i vx_i &= k^{-1} \sum_i x_i \\ v \sum_i x_i &= k^{-1} \sum_i x_i \\ v &= k^{-1}.\end{aligned}$$

Polynomial Functions. For a degree- d polynomial donor $P(\cdot)$, the equality $\bar{P}(vx) = P(x)$ must be satisfied, where $\bar{P}(\cdot)$ is the normalized version. The appropriate v is found from

$$\begin{aligned}\bar{P}(vx) &= P(x) \\ (vx)^d + \sum_{i=0}^{d-1} \bar{c}_i (vx)^i &= \sum_{i=0}^d c_i x^i \\ v^d x^d &= c_d x^d \\ v &= c_d^{1/d}.\end{aligned}$$

and the normalized coefficients are

$$\begin{aligned}\bar{P}(vx) &= P(x) \\ (vx)^d + \sum_{i=0}^{d-1} \bar{c}_i (vx)^i &= \sum_{i=0}^d c_i x^i \\ \bar{c}_i v^i x^i &= c_i x^i \\ \bar{c}_i &= c_i v^{-i} \quad \forall i \in \{0, \dots, d-1\}.\end{aligned}$$

Bivariate Polynomial. Assuming normalization along x , we require $\bar{S}(vx, y) = S(x, y)$ for the degree- d bivariate polynomial $S(x, y)$ and its normalization $\bar{S}(x, y)$. For that, v is determined from

$$\begin{aligned}\bar{S}(vx, y) &= S(x, y) \\ (vx)^d + \sum_{i=0}^{d-1} \sum_{j=0}^{d-i} \bar{c}_{ij} (vx)^i y^j &= \sum_{i=0}^d \sum_{j=0}^{d-i} c_{ij} x^i y^j \\ v^d x^d &= c_{d0} x^d \\ v &= c_{d0}^{1/d}.\end{aligned}$$

with the normalized coefficients being

$$\begin{aligned}\bar{S}(vx, y) &= S(x, y) \\ (vx)^d + \sum_{i=0}^{d-1} \sum_{j=0}^{d-i} \bar{c}_{ij} (vx)^i y^j &= \sum_{i=0}^d \sum_{j=0}^{d-i} c_{ij} x^i y^j \\ \bar{c}_{ij} v^i x^i y^j &= c_{ij} x^i y^j \\ \bar{c}_{ij} &= c_{ij} v^{-i} \quad \forall i \in \{0, \dots, d-1\}, \\ &\quad \forall j \in \{0, \dots, d-i\}.\end{aligned}$$

Receivers. Kernel Functions. Let $K(x) = \sum_{i \in I} w_i x_i + \beta$ and $\bar{K}(x) = \sum_{i \in I} \bar{w}_i x_i + \bar{\beta}$ be a kernel function and its updated version. To preserve model equivalence, we require $\bar{K}(x) = vK(x)$, thus

$$\begin{aligned}\bar{K}(x) &= vK(x) \\ \sum_{i \in I} \bar{w}_i x_i + \bar{\beta} &= v \left(\sum_{i \in I} w_i x_i + \beta \right) \\ \bar{w}_i x_i &= v w_i x_i \\ \bar{w}_i &= w_i v \quad \forall i \in I, \quad \bar{\beta} = \beta v.\end{aligned}$$

Polynomial Functions. For a degree- d polynomial receiver $P(x) = \sum_{i=0}^d c_i x^i$, the updated polynomial $\bar{P}(x) = \sum_{i=0}^d \bar{c}_i x^i$ must satisfy $\bar{P}(x) = vP(x)$. This yields

$$\begin{aligned}\bar{P}(x) &= vP(x) \\ \sum_{i=0}^d \bar{c}_i x^i &= v \sum_{i=0}^d c_i x^i \\ \bar{c}_i x^i &= v c_i x^i \\ \bar{c}_i &= c_i v \quad \forall i \in \{0, \dots, d\}.\end{aligned}$$

Bivariate Polynomial. For a degree- d bivariate polynomial $S(x, y) = \sum_{i=0}^d \sum_{j=0}^{d-i} c_{ij} x^i y^j$ and its updated version $\bar{S}(x, y) = \sum_{i=0}^d \sum_{j=0}^{d-i} \bar{c}_{ij} x^i y^j$, we require $\bar{S}(x, y) = \mathfrak{v}S(x, y)$. Therefore

$$\begin{aligned} \bar{S}(x, y) &= \mathfrak{v}S(x, y) \\ \sum_{i=0}^d \sum_{j=0}^{d-i} \bar{c}_{ij} x^i y^j &= \mathfrak{v} \sum_{i=0}^d \sum_{j=0}^{d-i} c_{ij} x^i y^j \\ \bar{c}_{ij} x^i y^j &= \mathfrak{v} c_{ij} x^i y^j \\ \bar{c}_{ij} &= c_{ij} \mathfrak{v} \quad \forall i \in \{0, \dots, d\}, \\ & \quad \forall j \in \{0, \dots, d-i\}. \end{aligned}$$

C Details on FHE Parameters

For each model, we detail the encryption parameters used in our experiments. Our framework automatically determines the RNS moduli according to the specified sizes $|q_i|$. We chose the smallest values of Δ and $|q_i|$ that preserve accuracy during private inference and adjust N for ≈ 128 -bit security. The moduli are ordered as q_0, \dots, q_L, P , where q_0 holds the output, q_1, \dots, q_L are for rescaling, and P is for modulus expansion in relinearization. FHE terminology is provided in §2.1.

VGG-16: $N = 2^{15}$, $\Delta = 2^{25}$, $\log_2 Q = 6 \cdot 50 + 10 \cdot 49 + 26 + 54 = 870$. Moduli: {0x4000000120001, 0x3ffffffdf0001, 0x40000001b0001, 0x3ffffffd20001, 0x4000000270001, 0x3ffffffcd0001, 0x20000000b0001, 0x20000001a0001, 0x1ffffff50001, 0x1ffffffea0001, 0x20000003b0001, 0x1ffffffd40001, 0x1ffffffba0001, 0x20000005e0001, 0x1ffffffb40001, 0x20000006d0001, 0x3ff0001, 0x3ffffffd60001}.

ResNet-18: $N = 2^{15}$, $\Delta = 2^{22}$, $\log_2 Q = 18 \cdot 44 + 23 + 54 = 869$. Moduli: {0x100000020001, 0x100000050001, 0x100000090001, 0x1000000b0001, 0xffffcf0001, 0x100000180001, 0x1000001a0001, 0xffffc60001, 0x1000002c0001, 0xffffb70001, 0x1000002d0001, 0x1000003c0001, 0xffffb50001, 0x1000003e0001, 0xffff-faf0001, 0x100000480001, 0xfffffac0001, 0x100000570001, 0x820001, 0x3ffffffd60001}.

ResNet-20: $N = 2^{15}$, $\Delta = 2^{21}$, $\log_2 Q = 20 \cdot 42 + 22 + 44 = 906$. Moduli: {0x400000b0001, 0x3ffffe80001, 0x400002f0001, 0x3ffffd20001, 0x40000330001, 0x3ffffca0001, 0x40000390001, 0x3ffffc30001, 0x400003b0001, 0x3ffffbe0001, 0x400004d0001, 0x3ffff850001, 0x40000560001, 0x400005c0001, 0x3ffff7b0001, 0x400006c0001, 0x3ffff550001, 0x40000770001, 0x3ffff4f0001, 0x400007a0001, 0x390001, 0x100000020001}.

ResNet-32: $N = 2^{16}$, $\Delta = 2^{26}$, $\log_2 Q = 32 \cdot 52 + 27 + 54 = 1745$. Moduli: {0x10000000060001, 0xfffffff00001, 0x1000000180001, 0xffffffe40001, 0x1000000200001, 0xffffffe20001, 0x100000003e0001, 0xfffffffbe0001, 0x10000000500001, 0xffffffa60001, 0x100000006e0001, 0xfffffff820001, 0x100000007e0001, 0xfffffff480001,

0x10000000960001, 0xfffffff280001, 0x10000000c80001, 0x10000000d80001, 0xfffffed60001, 0x10000000ec0001, 0xfffffec40001, 0x10000000fc0001, 0xfffffeb00001, 0x100000010e0001, 0xfffffe9e0001, 0x10000001380001, 0xfffffe9a0001, 0x100000016a0001, 0xfffffe940001, 0x10000001bc0001, 0xfffffe6a0001, 0x10000001be0001, 0x8020001, 0x3ffffffd60001}.